Chapter 2: Co-seismic phase: imaging the seismic rupture

Zacharie Duputel

Table des matières

Chapitre 2

Co-seismic phase: imaging the seismic rupture

2.1. Introduction

Most earthquakes correspond to a fault rupture inside the Earth. These phenomena are caused by the relative motion of tectonic plates on the terrestrial surface. When tectonic stresses increase and finally exceed the resistance of the fault, a rupture occurs with an abrupt deformation of the surrounding environment, releasing seismic waves (cf. Chapter 1). Although this description is generally correct, today we know that there are a variety of ways in which earthquakes occur [KAN 04a]. First of all, the size of earthquakes varies over several orders of magnitude. The smallest earthquakes last for only a fraction of a second, while the largest ruptures can occur over hundreds of kilometers in a few minutes. Furthermore, while earthquakes often correspond to 'brittle ruptures', releasing seismic waves, other, 'slow slip events' occur silently (cf. Chapter 7). Some earthquakes involve dissipative processes with a large amount of heat released. Others are not even caused by the fault tectonics but by large landslides or the activity of volcanoes.

This wide diversity of seismic sources observed in nature is still poorly understood. Why do some earthquakes stop quickly, after a few meters, while others continue to rupture a fault over several hundreds of kilometers? Why are some ruptures catastrophic, generating seismic waves, while others involve a slow slip over a fault? What is the interaction between the seismic and aseismic slip modes? Several models have been developed to try and explain the diversity of slip modes observed on faults. Over the past few decades, one dominant vision has consisted of considering faults as

Chapitre rédigé par Zacharie DUPUTEL, Observatoire Volcanologique du Piton de la Fournaise, Universite de Paris, Institut de Physique du Globe de Paris, CNRS, F-75005, Paris, France..

being segmented into large regions with different frictional properties that govern the seismic or aseismic character of slip [LAY 81]. This conceptual asperity model suggests an exclusive partitioning between slip modes and, notably, predicts the concept of "characteristic earthquakes" that always rupture the same asperity in a periodic fashion, predictable over time or with predictable slip (cf., Chapter 1). However, today we have many observation that suggest a superimposition between seismic and aseismic slips (see, for example [JOH 12]). Furthermore, a fault region may be entirely ruptured by a single large earthquake, but may also rupture sequentially, in a series of smaller earthquakes, as observed in Japan, Sumatra or in Ecuador [SIM 11, LAY 15, NOC 17]. This diversity is likely associated with a wide heterogeneity of frictional properties on faults (cf., Chapter 5), with conditionally stable slip zones to explain the occurrence of seismic ruptures in areas that are usually associated with slow continuous slip [SCH 98]. This spatial variability may also explain certain complex behaviors observed during the seismic cycle, such as the variability in the size of earthquakes in the same region [KAN 10].

In order to understand fault activity and rupture dynamics, we must characterize what happens during ruptures by determining the spatial and temporal slip behavior. We should then characterize the co-seismic slip and also the slip distributions associated with slow/transient deformations, and fault coupling in the inter-seismic period. Slip imaging makes it possible to evaluate the partitioning between seismic and aseismic slips, which is an essential parameter in seismotectonics since it determines the seismogenic potential of faults. The characterization of rupture processes is also important for the realistic simulation of strong motions generated by earthquakes. The seismic rupture is usually represented as a model describing the slip distribution over the fault, which are usually referred to as slip models or finite fault models. Since these models describe the rupture history without an explicit reference to the underlying forces, they are also called kinematic models. The estimation of slip models is complicated by observational noise, the complexity of rupture processes, and our limited knowledge of the Earth structure. Since the pioneering work carried out in the 1970s, different approaches have been developed to obtain images of the spatio-temporal distribution of fault slip. The 1971 San Fernando earthquake($M_W = 6.7$, California) is the first earthquake for which a slip model could be established using seismological data [TRI 74]. Today, slip models are routinely calculated for every large earthquake, which is facilitated by the rapid availability of a large volume of data. The increase in computation capabilities has also led to significant improvements, especially with respect to solving non-linear problems and simulating waveforms in complex media.

Slip inversion methods are the central theme of this chapter. Chapter 2 discusses the determination of first-order characteristics of earthquakes (focal mechanism, source function etc.). Here, we will first summarize the main types of data used today in seismic rupture imaging. Next, we will examine the forward problem, i.e., the formulation to predict surface observations for a given seismic source. We will then approach the inverse problem, consisting of finding the slip distribution from surface

data. Finally, we will discuss certain implications of slip models on the dynamics of seismic ruptures.

2.2. Surface observations

The amount of measurements available to study earthquake sources has evolved considerably over the last few decades. In this section, we summarize the main geophysical data used today to image the seismic rupture. In particular, we will examine in details the seismological data that is an essential ingredient in determining the temporal evolution of slip. These observations are generally associated with different types of geodetic data (GNSS, high-rate GNSS, radar interferometry, image correlation). Tsunami data can also bring significant constraints in rupture areas located offshore. In addition to these measurements, earthquake studies have also benefited from field observations. These observations make it possible, for example, to map the trace of faults or even directly measure slip at the surface.

2.2.1. *Seismological data*

Seismometers are the most widely-used instrument for quantifying seismic displacements. These sensors are made up of a mass attached to the ground through a spring and a damping device. For a long time, ground movement was measured through the displacement of the mass relative to the ground. Modern instruments are based on the same inertial system, but with an electromagnetic feedback mechanism that prevents the mass from moving. The correction signal required to prevent the mass from moving is recorded. This system makes it possible to have a compact instrument recording signals over a large range of frequencies and amplitudes, conserving the linearity of the sensor. For more information on seismometry, the reader may consult Chapter 12 of [AKI 02].

Seismological waveforms provide essential information to estimate the time history of seismic ruptures. Two types of seismological sensors are widely used today to characterize the seismic source: broadband seismometers and strong motion sensors. Seismological data may be seen as the convolution product of ground displacement in the recorded direction and the sensor's transfer function. Thus, in the frequency domain, the seismological recordings $S(\omega)$ may be described as:

$$S(\omega) = I_D(\omega)U(\omega) \tag{2.1}$$

where ω is the angular frequency, $U(\omega)$ is the ground displacement, and $I_D(\omega)$ is the displacement transfer function of the sensor. Alternatively, the instrument response with respect to the ground displacement velocity ($I_V(\omega)$) or to its acceleration ($I_A(\omega)$) can be used in the above equation $S(\omega) = I_V(\omega)\dot{U}(\omega) = I_A(\omega)\ddot{U}(\omega)$

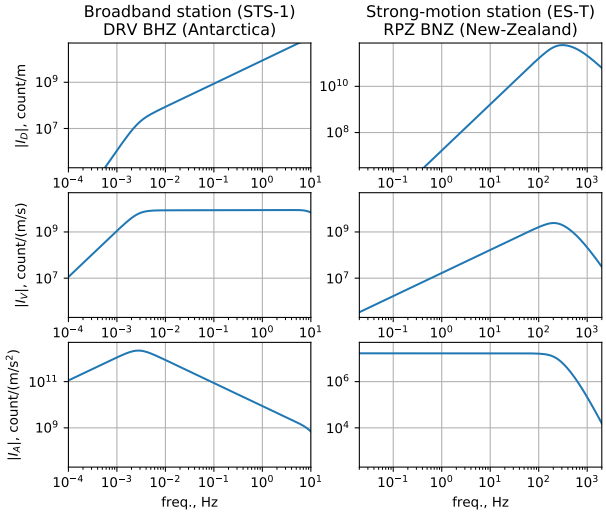

Figure 2.1. Examples of instrumental responses for a broadband seismometer (left) and for an accelerometer (right). *The spectral amplitude of transfer functions in displacement I_D, velocity I_V, and acceleration I_A is shown for each case. The broadband station is equipped with a Streckeisen STS-1 sensor, with a corner frequency at 2.7mHz. The strong motion sensor is an EpiSensor (ES-T) kinemetrics accelerometer with a corner frequency at 200 Hz. Both of these sensors are force-feedback sensors.*

where $\dot{U}(\omega)$ and $\ddot{U}(\omega)$ correspond, respectively, to the ground velocity and acceleration. Figure 2.1 presents the responses of a broadband seismometer (Dumont d'Urville station in Antarctica) and a strong motion sensor in New Zealand. The broadband instrument presents a velocity transfer function ($I_V(\omega)$) that is almost flat over a large frequency range, that is, a response that is proportional to ground velocity up to a period of 360 s. For longer periods, the amplitude of the instrumental response decreases proportional to ω^2. The strong motion sensor depicted in Figure 2.1 is an accelerometer, that is, it has a 'flat' acceleration response from zero frequency up to its corner frequency (here 200 Hz).

In order to work with data that can be physically interpreted, the recorded signals must be corrected from the instrumental response. For example, if we wish to extract the ground displacement:

$$U(\omega) \sim F(\omega)\frac{S(\omega)}{I_D(\omega)} \tag{2.2}$$

During this deconvolution, we use a filter $F(\omega)$ that filters the data in a pass band similar to the one that is used for inversion.

Figure 2.2 presents examples of signals that were recorded during the 2016 Kaikoura earthquake (New Zealand, $M_W = 7.8$) by the broadband station DRV (the Dumont d'Urville station in Antarctica) and the strong-motion station RPZ (Rata Peaks in New Zealand), whose responses are depicted in Figure 2.1. The raw data is on top, and the data after instrument correction is presented below (for ground displacement velocity and acceleration). It can be clearly seen that the acceleration and velocity data have higher frequency than the displacement data. This effect is related to the time derivative relationship between these signals, translated by a factor $i\omega$ in the spectral domain (where i is the imaginary unit). Acceleration or velocity waveforms are therefore more sensitive to rupture complexities visible at high frequency. This data is also more sensitive to heterogeneities in the propagation medium, which are not necessarily adequately considered in the velocity model that is employed for slip inversion. In practice, we often use displacement or velocity data (since ground acceleration is usually difficult to model).

As broadband stations are very sensitive to ground displacement, they make it possible to observe seismic waves over large distances (over 3000 km from the epicenter in Figure 2.2). At these teleseismic distances, body waves are conventionally used (generally P and SH waves) to determine the time history of the rupture. In Figure 2.2 on the left, the teleseismic P waves emerge weakly until there is a large amplitude arrival around 60 s after the first arrival. This arrival corresponds to large slip that occurred $\sim$60 s after the earthquake origin time in the northern part of the Kaikoura earthquake rupture (see, for example [WAN 18]). We can also use surface waves (Rayleigh and Love waves) which can constrain first-order source parameters such as the seismic moment and rupture directivity (see, for example [DUP 17]). Unlike broadband seismometers, accelerometers are usually much less sensitive (cf. Figure 2.1), allowing us to record very strong motions without data clipping. On the right of Figure 2.2, we once again see that the signal emerges weakly and that the energetic arrivals come later ($\sim$60 s after the first arrival as in teleseismic data). For more details on seismological data recorded at global and regional scales, the reader is referred to Chapter 2.

2.2.2. *GNSS data: from geodesy to seismo-geodesy*

GNSS (Global Navigation Satellite System) data is among the most-widely used data to study earthquakes. This includes the Global Positioning System (GPS), the Russian system GLONASS or the European Galileo system. By estimating the position of a point with respect to a reference system defined by a constellation of satellites, this data allows the measurement of co-seismic displacements in three directions (vertical, east and north). Two types of measurements may be acquired: campaign measurements or measurements from continuous stations. In the first case, the measured displacements may contain a large part of the inter-seismic and post-seismic

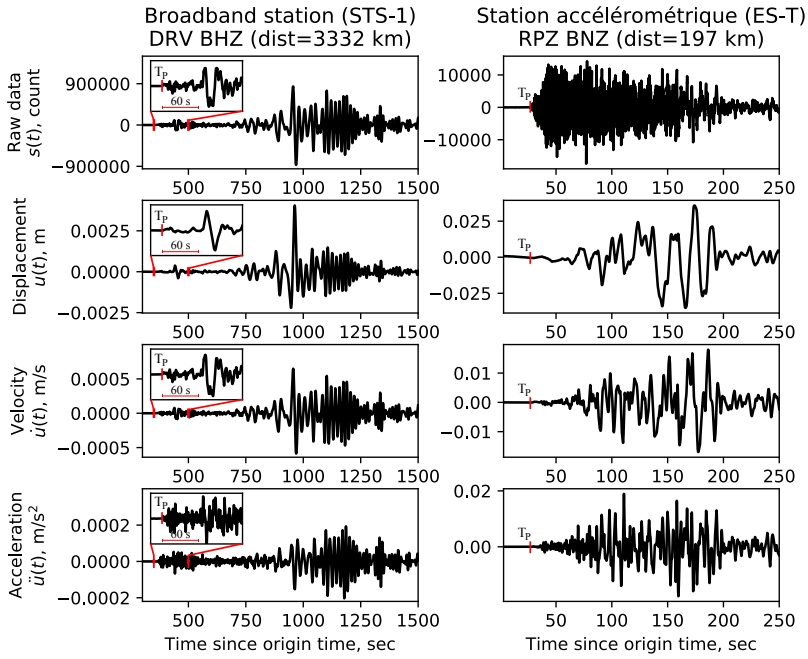

Figure 2.2. Seismological recordings during the 2016 Kaikoura earthquake ($M_W = 7.8$, New Zealand). *The waveforms presented here correspond to the broadband seismometer (STS-1, on the left) and to the accelerometer (EpiSensor ES-T) whose responses are given in Figure 2.1. In each case, we show the raw data, $s(t)$, the displacement data $u(t)$, the velocity data $\dot{u}(t)$ and the acceleration data $\ddot{u}(t)$. The correction of the instrumental response is carried out between periods of 5 and 125 s (0.008-0.2 Hz). The insets on the left of the figures show an enlargement of the teleseismic P arrival at the DRV station (T_P indicates P-wave arrival times).*

displacements, or motions related to aftershocks, which may be corrected by combining the observations with other available data (see, for example [KLE 17]). In the case of measurements from continuous stations for which a daily position is estimated, co-seismic displacements can be estimated from the offset between the estimated positions before and after the event. Daily co-seismic data may also be affected by the post-seismic deformations [TWA 19] or by the earthquakes occurring immediately before or after the mainshock [SIM 11].

Along subduction zones, on land geodetic data is almost insensitive to deformation processes off the coast. To mitigate this problem, several seafloor geodetic approaches have been developed from the 1980s onwards [BÜR 14]. One approach in particular, combining GNSS observations and acoustics ranging (GNSS-A) is used today in

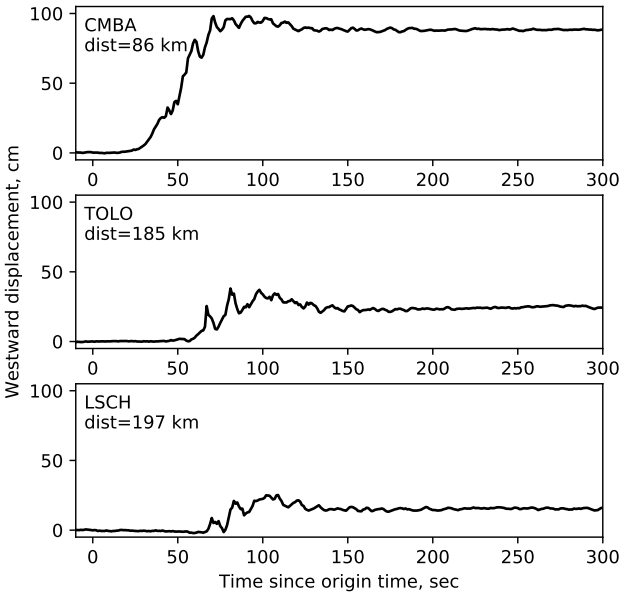

Figure 2.3. High-frequency GNSS displacements during the 2015 Illapel earthquake in Chile ($M_W = 8.3$). *The westward displacements are presented for three GPS stations at various epicentral distances (indicated in each case). The time-series sampled at 1 Hz were obtained at the Jet Propulsion Laboratory using the GIPSY-OASIS code in Precise Point Positioning mode (data processed by S. Owen, A. Moore and M. Simons).*

various regions [YOK 20]. This method is based on the GNSS positioning of a boat (or an autonomous robot) from which the transponders placed on the seafloor are located through acoustic ranging. Another widespread method is the deployment of pressure sensors that measure vertical displacements. Many other approaches have also been suggested, such as the installation of seafloor inclinometers, repetitive SONAR mapping, or fiber optic deformation measurement [BÜR 14].

Over the last decade, there have also been significant efforts to obtain GNSS measurements sampled at higher frequency (i.e., $\geq$1 Hz, [LAR 03]). With such sampling, these measurements correspond, in reality, to seismograms but there are three main differences: (1) high-rate GNSS data directly measures the ground displacement, which eliminates the problem of the integration of seismological data (2) there is no waveform clipping (unlike conventional seismograms), (3) GNSS stations are much less sensitive to seismological data (which limits their use to the largest earthquake at small epicentral distances). An example of high-rate GNSS data is presented in Figure 2.3 for the 2015 Illapel earthquake (Chile, $M_W = 8.3$). We can clearly see the superimposition of the dynamic wave field (short period oscillations) and the static

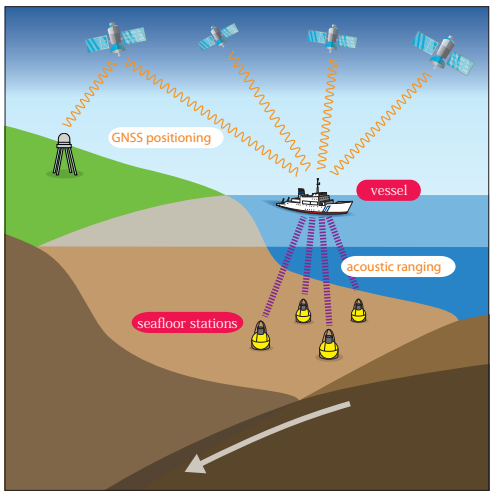

Figure 2.4. The GNSS-A seafloor geodesic observation system. *This system combines the GNSS positioning of a boat (or an autonomous robot) and acoustic ranging for the relative positioning of transponders placed on the seafloor. This figure is modified according to [YOK 20].*

displacement (long-period ramp). this data is very useful in the near field as it yields information on both the final slip and the rupture time history.

2.2.3. *Satellite and aerial imaging*

Data from satellite and aerial imaging has considerably improved our view of the deformation field associated with active faults. Satellite data is especially useful as it gives us a global view of the surface deformation, even in regions that are poorly equipped with instruments. These imaging methods are based on the combination of satellite or aerial images acquired before and after the earthquake being studied. In addition to the co-seismic signal, these measurements may contain a non-negligible part of inter- and post-seismic signals along with displacements induced by after-shocks (cf., Chapters 1 and 4).

Radar interferometry is particularly useful to measure the displacement field generated by earthquakes [MAS 93, SIM 07]. This approach is based on the use of two SAR (*Synthetic-Aperture Radar*) images taken before and after an earthquake. The SAR images are obtained by emitting a series of electromagnetic pulses from a lateral antenna on a satellite or airborne system [SIM 07]. The echoes of each pulse are combined to obtain an image of the observed zone. By measuring the phases differences for each point captured before and after an earthquake, it is possible to generate a

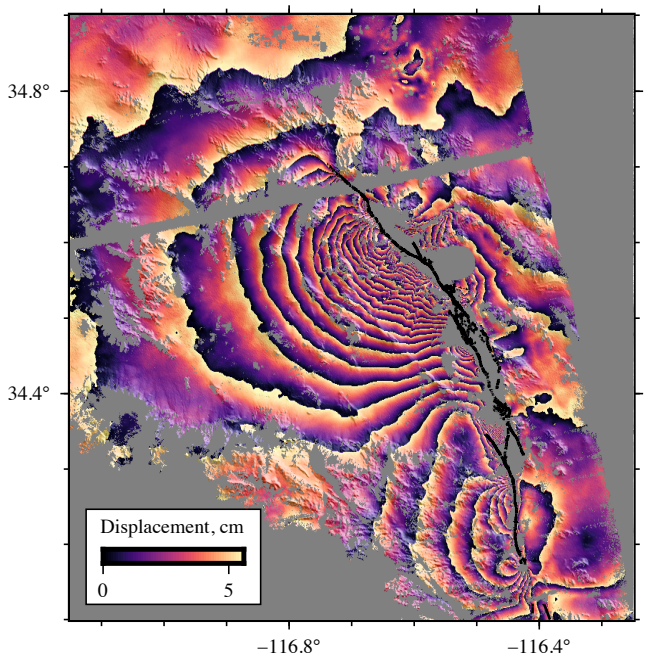

Figure 2.5. Interferogram showing the deformation associated with the 1992 Landers earthquake (California, $M_W = 7.2$). *This data has been obtained from two SAR images acquired by the ERS-1 satellite in an ascendant orbit on 26th May and 30th June 1992 (cf. [GOM 18a]). The colors indicate the displacement measured in the satellite's line-of-sight. The phase was unwrapped and then re-wrapped at 5.17cm per fringe. The fault trace of the Landers earthquake is shown in black.*

map of the co-seismic displacement in the line-of-sight of the satellite. This method is commonly called InSAR for *Interferometric Synthetic-Aperture Radar*. It must be noted that when the displacement is too large, InSAR data suffers from a loss of coherence, which can sometimes affect measurements in the vicinity of the rupture. Many sources of noise may also contaminate InSAR data. In particular, the atmosphere and ionosphere can induce propagation delays to the SAR signal resulting into phase shifts in the interferogram (e.g., due to variations in tropospheric water vapor content). The amplitude of these errors can be large and can sometimes even exceed the tectonic signal. While the ionospheric effect is more difficult to estimate, several techniques have been developed to evaluate the signal originating in the troposphere and to correct for these effects in the interferogram (see, for example, [JOL 11]). Another source of noise is due to the poor knowledge of the satellite orbit, inducing a large-wavelength signal in the image. An orbital correction can thus be estimated to limit the impact on slip models [SIM 07].

Figure 2.5 shows an example of an InSAR image of the 1992 Landers earthquake ($M_W = 7.2$). This was the first earthquake imaged using radar interferometry [MAS 93]. The image is dominated by the co-seismic displacement associated with the mainshock, but also includes 2 days of post-seismic deformation as well as an aftershock of magnitude $M_W = 6.5$, which occurred a few hours after the mainshock (to the south in the image).

Another widely used approach is the correlation of images taken before and after an earthquake. These images may correspond to optical satellite images [AVO 14], to aerial photographs [GOM 18a] or again, to SAR amplitude images [SIM 07]. Unlike with SAR, which illuminates the zone under study, cloud cover is a limiting parameter when optical images are used. Although this method is not very sensitive to atmospheric disturbances, the main difficulties are due to the co-registration of two images along with orbital nuisances that may affect one or both images. The correlation of images is a method that is complementary to InSAR as it inform us about horizontal displacements and can also provide measurements close to faults, where InSAR often suffer from incoherent phase returns.

2.2.4. *Tsunami data*

Subduction earthquakes can generate large displacements of the seafloor. Such large seafloor motions result in a change of the sea-level with respect to its equilibrium, thus creating tsunami waves. Tsunami data is therefore a significant asset as it provides important information on the seafloor displacements, where few observations are available.

Tsunami data are measured by estimating variations in height of the ocean surface. From the 2000s onwards, a network of DART (*Deep-ocean Assessment and Reporting of Tsunamis*) buoys has been deployed in the open sea by NOAA (*National Oceanic and Atmospheric Administration*). These buoys transmit real-time recordings from a pressure sensor placed on the seafloor, to estimate variations in the height of the water column. Tsunamis can also be recorded on the coast using tide gauges, providing data which is generally more sensitive to local bathymetry. Other tools can also be used. In 2004, for example, the Jason altimetry satellite was able to measure the tsunami generated by the Sumatra-Andaman earthquake ($M_W = 9.0$, [SLA 08])

2.3. The Forward Problem

We will now introduce the formulation to relate the earthquake source to surface observations (listed in section 2.2). We consider that a seismic rupture corresponds to a displacement discontinuity $\Delta\mathbf{u}(\boldsymbol{\xi}, \tau)$ over a duration T through one or more faults corresponding to a surface denoted by Σ. The function $\Delta\mathbf{u}(\boldsymbol{\xi}, \tau)$ thus describes the

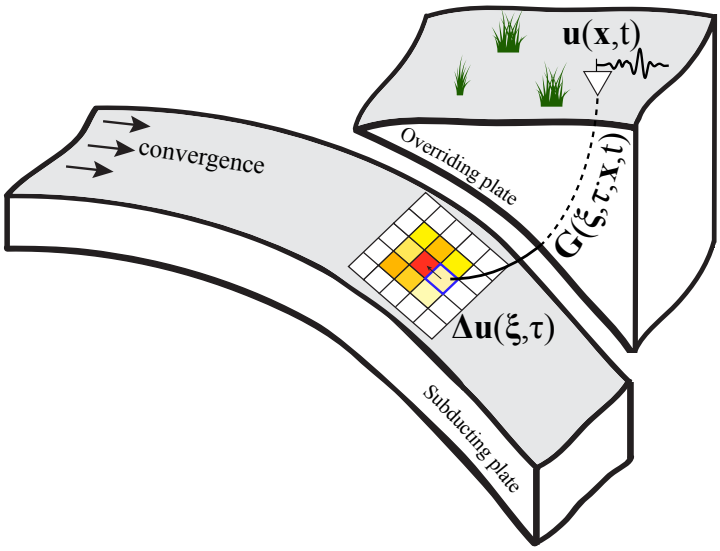

Figure 2.6. Forward problem in the case of a subduction earthquake. *In this example, the fault is spatially discretized with rectangular sub-faults (here colored according to the amplitude of slip). The slip distribution $\Delta\mathbf{u}(\boldsymbol{\xi},\tau)$ in space ($\boldsymbol{\xi}$) and in time (τ) is linked to surface observations $\mathbf{u}(\mathbf{x},t)$ using the Green's function $\mathbf{G}(\mathbf{x},t;\boldsymbol{\xi},\tau)$ as indicated in equation 2.3. Figure modified as per [GOM 18c]*

slip over time (τ) and space ($\boldsymbol{\xi}$) on the considered fault (voir Figure 2.6). It is also assumed that over the considered timescale, the medium behaves in a linear elastic manner. The displacement discontinuity $\Delta\mathbf{u}(\boldsymbol{\xi},\tau)$ over the fault Σ may thus be related to the observed displacement $\mathbf{u}(\mathbf{x},t)$ via the following expression:

$$u_i(\mathbf{x},t) = \int_0^T d\tau \int_\Sigma \Delta u_j(\boldsymbol{\xi},\tau)\, c_{jkpq}(\boldsymbol{\xi})\, \nu_k(\boldsymbol{\xi})\, G_{ip,q}(\mathbf{x},t;\boldsymbol{\xi},\tau)\, d\Sigma \tag{2.3}$$

where G_{ip} is the Green's function describing the displacement component i at the receiver at $(\mathbf{x},t)$ due to an impulse force at $(\boldsymbol{\xi},\tau)$ acting in the direction p. The index q in $G_{ip,q}$ indicates the derivative of the Green's function G_{ip} with respect to direction ξ_q. In this equation we also have the elastic constants c_{ijpq} and the normal to the fault surface $\boldsymbol{\nu}(\boldsymbol{\xi})$. We will restrict ourselves here to the case where the displacement discontinuity $\Delta\mathbf{u}(\boldsymbol{\xi},\tau)$ is perpendicular to $\nu(\boldsymbol{\xi})$. For more details on this representation of the seismic source, the reader can refer to Chapters 2 and 3 in [AKI 02]. Equivalently, we can rewrite equation (2.3) as :

$$u_i(\mathbf{x},t) = \int_0^T d\tau \int_\Sigma \Delta\dot{u}_j(\boldsymbol{\xi},\tau)\, c_{jkpq}(\boldsymbol{\xi})\, \nu_k(\boldsymbol{\xi})\, H_{ip,q}(\mathbf{x},t;\boldsymbol{\xi},\tau)\, d\Sigma \tag{2.4}$$

where $\Delta\dot{\mathbf{u}}$ is slip velocity and $H_{ip,q}$ is the Earth response to a step function:

$$H_{ip,q}(\mathbf{x}, t; \boldsymbol{\xi}, \tau') = \int_0^{\tau'} G_{ip,q}(\mathbf{x}, t; \boldsymbol{\xi}, \tau)\, d\tau. \tag{2.5}$$

We wish to describe slip distribution in time and space. This is done by parametrizing the slip velocity by decomposing it over N_s spatial basis functions in the following manner [IDE 07]:

$$\Delta\dot{u}_i(\xi, \tau) = \sum_{j=1}^{N_s} p^j\, \hat{u}_i^j(\tau)\, \phi^j(\xi)\, h^j(\xi, \tau) \tag{2.6}$$

where we define:
– $\Delta\dot{u}_i$ the i-th component of the slip velocity vector on the fault,
– $\phi^j(\xi)$ the j-th spatial basis function associated with the coefficient p^j,
– p^j a coefficient whose dimension is the product of slip and area,
– $h^j(\xi, \tau)$ a function describing the temporal evolution of the rupture,
– $\hat{u}_i^j(\tau)$ a unit vector representing slip direction at time τ.
The functions $\phi^j(\xi)$ et $h^j(\xi, \tau)$ are normalized so that $\int\int_\Sigma \phi^j(\xi) d\Sigma(\xi) = 1$ and $\int_{-\infty}^{+\infty} h^j(\xi, \tau)\, d\tau = 1$.

A common choice for the spatial parametrization of the slip is to normalize the fault with sub-faults in which the slip is considered constant at a given time. Rectangular sub-faults (as in Figure 2.6) or triangular sub-faults are commonly used in literature. In the previous equations, we thus define $\phi^j(\mathbf{x})$ as a function carried on the fault. For the j-th sub-fault, we then have

$$\begin{aligned} &\phi^j(\xi) = 1/\Sigma^j \text{ when } \xi \in \Sigma^j \\ &\phi^j(\xi) = 0 \text{ otherwise} \end{aligned} \tag{2.7}$$

where Σ^j corresponds to the surface of the sub-fault j. In this case, the coefficients p^j correspond directly to the product of the slip and the area of each sub-fault, which is commonly referred to as "seismic potency". Alternatively, one may define $\phi^j(\xi) = 1$ in Σ^j so that p^j corresponds directly to average slip in the j-th subfault.

2.3.1. *The Static Case: modeling geodetic data*

If we are only interested in the final slip distribution, we can use co-seismic geodetic data, which is only sensitive to the static slip distribution. For moderate sized earthquakes, this also includes tsunami data, as it has low sensitivity to rupture history. Earthquakes of magnitude $M_W > 8$ have a long rupture duration ($T > 1$ min),

which must generally be taken into account when modeling tsunami data. Static data is modeled by integrating previous equations over time up to the rupture duration T. We then obtain:

$$\Delta u_i(\xi) = \sum_{j=1}^{N_s} p^j \, \hat{u}_i^j \, \phi^j(\xi) \tag{2.8}$$

where $\hat{u}_i^j$ represents the final direction of slip over the fault. It is then possible to decompose the slip vector into two components:

$$\Delta u_i(\xi) = \sum_{j=1}^{N_s} (p^{j1} v_i^1 + p^{j2} v_i^2) \, \phi^j(\xi) \tag{2.9}$$

where p^{j1} and p^{j2} are the components of $p^j \hat{u}_i^j$ in the direction of the two unit orthogonal vectors $\mathbf{v}^1$ and $\mathbf{v}^2$. For example, $\mathbf{v}^1$ and $\mathbf{v}^2$ can correspond to directions along the fault dip and along the fault azimuth. By replacing this formulation in equation (2.3), we obtain:

$$u_i(\mathbf{x}) = \sum_{l=1}^{N_s} (p^{l1} v_j^1 + p^{l2} v_j^2) \, \mathcal{G}_{ij}^l(\mathbf{x}) \tag{2.10}$$

where:

$$\mathcal{G}_{ij}^l(\mathbf{x}) = \int \int_{\Sigma} \phi^l(\xi) \, c_{jkpq}(\xi) \, \nu_k(\xi) \, G_{ip,q}(\mathbf{x}; \xi) \, d\Sigma(\xi) \tag{2.11}$$

In the case where a sub-fault parametrization is used, we have:

$$\mathcal{G}_{ij}^l(\mathbf{x}) = \frac{1}{\Sigma^l} \int \int_{\Sigma^l} c_{jkpq}(\xi) \, \nu_k(\xi) \, G_{ip,q}(\mathbf{x}; \xi) \, d\Sigma(\xi) \tag{2.12}$$

where Σ^l corresponds to the area of the sub-fault l for which $\phi^l(\xi) = 1/\Sigma^l$ (see equation 2.7). In the above equations, $\mathcal{G}_{ij}^l(\mathbf{x})$ describes the surface displacement (at $\mathbf{x}$) caused by a unit slip over sub-fault l. In a homogeneous half-space, this function can be calculated analytically [OKA 85]. For a heterogeneous medium, there are various tools to numerically calculate the response of a tabular medium (e.g. [ZHU 02]) or a 3D medium (e.g. [AAG 13]).

In the static case, it is thus possible to describe the final slip distribution using two slip potency components, p^{l1} and p^{l2}, for each sub-fault l (i.e, for each basis function ϕ^l). This is a linear problem:

$$\mathbf{d}_s = \mathbf{G}_s \, \mathbf{m}_s \tag{2.13}$$

where $\mathbf{d}_s$ is the data vector containing the geodesic surface measures, $\mathbf{m}_s$ corresponds to the model vector containing the coefficients p^{l1}, and p^{l2}, $\mathbf{G}_s$ is the matrix containing the functions $\mathcal{G}_{ij}^l(\mathbf{x})$ defined in equations 2.11 and 2.12).

2.3.2. *The kinematic case: modeling seismological data and high-frequency GNSS data*

If we wish to examine how ruptures propagate along the faults, we must choose the parametrization that will describe the temporal evolution of slip. Traditionally, there are two approaches, which are detailed below.

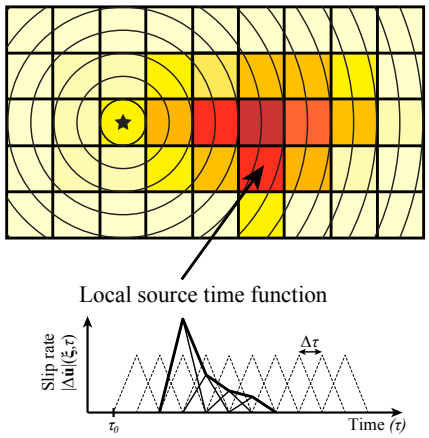

Figure 2.7. Multiple time window parametrization. *Example of a formulation based on the use of triangular basis functions in time and rectangular basis functions in space. The color of each sub-fault indicates the amplitude of slip. The minimum rupture times τ_0 are shown by time isocontours on the fault. The slip velocity is presented in black for one of the sub-faults after summing up the time functions (dotted triangles).*

2.3.2.1. *Linear approaching using multiple time windows*

As depicted in Figure 2.7, a parametrization using multiple windows consists of expanding the function $\hat{u}_i^j(\tau)\, h^j(\xi,\tau)$ in equation (2.6) using a series of N_t coefficients:

$$\Delta\dot{u}_i(\xi,\tau) = \sum_{j=1}^{N_s}\sum_{k=1}^{N_t}(p^{jk1}v_i^1 + p^{jk2}v_i^2)\,\phi^j(\xi)\, f(\tau-(k-1)\Delta\tau-\tau_0(\xi)) \quad (2.14)$$

In this equation, $f(\tau)$ is a temporal basis function that is zero for $\tau < 0$ with unit integral and a finite support. A typical choice for $f(\tau)$ is a boxcar function or a triangular function [OLS 82]. These functions represent a series of windows all spaced apart by $\Delta\tau$ between a minimum rupture time $\tau = \tau_0(\xi)$ and a maximum rupture time $\tau = \tau_0(\xi) + (N_t - 1)\Delta\tau$. This parametrization thus decomposes the slip velocity $\Delta\dot{\mathbf{u}}$ into a series of coefficients p^{jkl} associated with the l-th direction of slip over the j-th spatial basis function, and a time window offset by $(k-1)\Delta\tau+\tau_0(\xi)$ (see Figure 2.7).

Substituting this equation in (2.3) yields an expression that is quite similar to the static case. By considering a rectangular function $\phi^j(\xi)$ for the j-th sub-fault and an initial rupture time $\tau_0(\xi \in \Sigma^j) = \tau_0^j$:

$$u_i(\mathbf{x},t) = \sum_{l=1}^{N_s}\sum_{k=1}^{N_t}(p^{lk1}v_j^1 + p^{lk2}v_j^2)\,\mathcal{G}_{ij}^{lk}(\mathbf{x}, t-(k-1)\Delta\tau - \tau_0^j) \tag{2.15}$$

with:

$$\mathcal{G}_{ij}^{lk}(\mathbf{x},t) = \frac{1}{\Sigma^l}\int_0^T d\tau \int\int_{\Sigma^l} f(\tau)\, c_{jkpq}(\xi)\, \nu_k(\xi)\, H_{ip,q}(\mathbf{x},t;\xi,\tau)\, d\Sigma(\xi) \tag{2.16}$$

As in the static case, we obtain a linear problem:

$$\mathbf{d}_k = \mathbf{G}_k\mathbf{m}_k \tag{2.17}$$

where $\mathbf{d}_k$ is the data vector, $\mathbf{m}_k$ includes the coefficients p^{jkl}, and $\mathbf{G}_k$ is the matrix containing the waveforms calculated for each basis function in space and in time (cf., equation 2.16).

This parametrization is often used as it results in a system of linearized equations that can be resolved using conventional approaches such as the least squares method. The multiple time window model is also advantageous because it allows some flexibility in the slip time history. However, one major drawbacks of this formulation is that it relies on a large number of parameters to be estimated. For large earthquakes occurring over large faults, with long rupture durations, there can easily be several thousands of parameters. To reduce the dimension of the problem, we generally consider a limited number of time windows starting from a minimum rupture time $\tau_0(\xi) = |\xi - \xi_0|/V_R^{max}$, determined by a rupture velocity V_R^{max} and the position of the hypocenter ξ_0 on the fault (which is fixed *a priori*).

2.3.2.2. *Non-linear approach*

In the non-linear approach to kinematic inversion, rupture times are treated as parameters to be determined. We thus have:

$$\Delta\dot{u}_i(\xi,\tau) = \sum_{j=1}^{N_s}(p^{j1}v_i^1 + p^{j2}v_i^2)\,\phi^j(\xi)\, f(\tau-\tau^j, r^j) \tag{2.18}$$

with:

– $f(\tau, r)$ being a function that is zero for $\tau < 0$ and $\tau > r$ and with unit integral,
– τ^j corresponding to the rupture time for sub-fault j (or the function ϕ^j),
– r^j is the local duration of slip, called 'rise-time'.

In the non-linear approach, the shape of the local source function $f(\tau, r)$ is identical for all sub-faults (unlike the multiple time window linear approach). It is possible to

use different shapes for the function $f(\tau, r)$: boxcar and triangular functions are the typical choices (cf., Figure 2.8). It is also possible to use expressions that best represent the rupture dynamic (e.g., a Yoffe function is depicted in Figure 2.8, [TIN 05b]).

By integrating this parametrization into equation (2.3), we obtain a non-linear forward problem:

$$\mathbf{d}_k = \mathbf{G}_k(\mathbf{m}_k) \tag{2.19}$$

In this equation, the model vector $\mathbf{m}_k$ includes the coefficients p^{jl}, the rise time r^j and rupture time τ^j. $\mathbf{G}_k$ represents the non-linear function that relates these parameters to the data vector $\mathbf{d}_k$. Some approaches describe the rupture velocity V_R^j in each sub-fault instead of the rupture time τ^j (see, for example [MIN 13]). The forward calculation $\mathbf{G}_k(\mathbf{m}_k)$ then includes the solution to the eikonal equation

$$|\nabla \tau^j| = 1/V_R^j \tag{2.20}$$

to derive the rupture times τ^j (with $\tau^j = 0$ at the hypocenter of the earthquake) from the rupture velocities V_R^j. This kind of approach is particularly useful to impose the causality of the rupture front.

A non-linear parametrization allows to significantly reduce the dimension of the problem. Using this formulation, the number of parameters is $4 \times N_s$, which is generally much lower than the $2 \times N_s \times N_t$ parameters used in the multiple time window approach (cf. equation 2.15). A major drawback is the non-linear nature of the forward problem, which complicates the solution of the inverse problem and may lead to the existence of local minima.

2.3.3. *Computing the Green's functions*

The formulations of the forward problem given above are based on the spatial derivatives of the Green's functions (i.e., $G_{ip,q}$ and $H_{ip,q}$ in equations 2.3 and 2.4) which must be calculated at every point of the fault. Different strategies may be used for that purpose depending on the parametrization and data used.

As described in section 2.3.1 for the static case, there are analytical solutions to calculate the Green's functions in a homogeneous half-space [OKA 85]. There are also different numerical tools to simulate the static displacements in a 2D or 3D medium [ZHU 02, AAG 13]. When tsunami data is used, these static Green's functions must be coupled with models describing tsunami propagation for a given displacement field on the seafloor [SAT 07]. Since the tsunami wavelength is generally much greater than the depth of the water and its amplitude is small compared to the ocean depth in open sea, tsunami modeling is usually carried out by considering approximations called 'shallow water' and 'small-amplitude wave' conditions. One of the most popular codes based on these approximations is COMCOT (COrnell Multi-grid COupled Tsunami Model

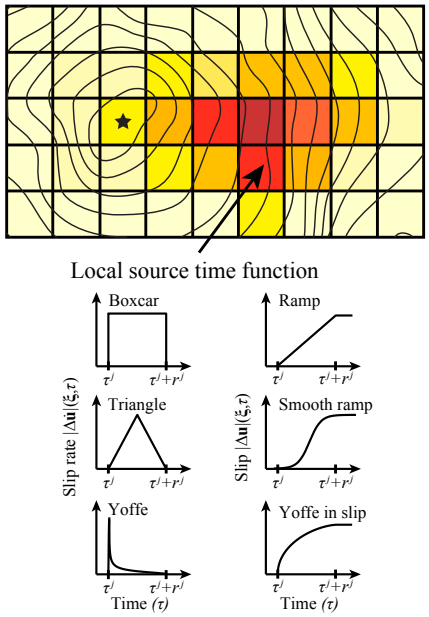

Figure 2.8. Non-linear parametrization. *Non-linear formulation where the temporal evolution of slip is parametrized with a rupture time τ^j and a rise time r^j. We consider a sub-fault spatial parametrization where the color indicates the amplitude of the slip. The rupture times are indicated on the fault using isocontours. Different choices for the function $f(\tau, r)$ are presented below in terms of slip velocity on the left (boxcar, triangular and Yoffe functions) with their equivalent in slip on the right (linear ramp, smooth ramp, Yoffe function in slip).*

[LIU 98]). Although this code is well suited to model DART data in the open ocean, it is not appropriate for coastal tide-gauge data, for which the small-amplitude wave hypothesis is often not valid. In addition, dispersive effects related to the elasticity of the seafloor and to variations in water density are generally neglected [TSA 13]. These effects can cause delays up to several minutes in tsunami propagation. Codes have been developed to model these effects [ALL 14] and it is also possible to apply first-order corrections to the travel time [TSA 13] or to the oceanic depth [INA 13].

The modeling of seismological data is generally based on the simulation of waveforms for a tabular medium. Teleseismic data is generally modeled using the propagator matrix method coupled with ray theory [BOU 76, KIK 91]. The teleseismic P and S waves are thus modeled by considering the tabular media at the source, at the receivers and at the points of reflection of PP waves if these phases are used. To predict seismic waveforms at near field distances, it is common to use methods based on the

wavenumber integration approach [BOU 81], which is available in several widely distributed codes (e.g., [HER 13]). It is increasingly more common in studying seismic sources to take into account the 3D structure [HJÖ 09]. This can be done using different 3D waveform simulation methods, such as the finite difference method or spectral elements method [KOM 99]. Although it is important to consider lateral heterogeneities to improve the characterization of the source, detailed models of the 3D structure are not always available. In order to minimize the impact of any imprecision in the Earth model, certain approaches are based on the empirical calibration of Green's functions [WEI 13]. A good alternative is to use empirical Green's functions (EGF), which consists of using recordings of small earthquakes that are co-located with the earthquake being studied [HAR 78]. Nonetheless, EGF coverage is not always sufficient to cover the entire fault and this approach is based on the hypothesis that the earthquake being studied and the EGFs are associated with the same focal mechanism. The question of modeling the seismic wave field (especially at teleseismic distances) is described in greater detail in Chapter 2.

Imprecisions in the velocity model used to calculate Green's functions can have a large impact on slip inversion results. As described in the following section, the uncertainty associated with the Earth model can be taken into account in the inverse problem. In order to mitigate the impact of inaccuracies in the velocity model, a common practice is to align predicted and observed wave arrivals to minimize differences between the corresponding seismic phases. However, this approach remains complex in the near field since S waves arrivals are often masked by P waves for large earthquakes. A poor alignment of P and/or S arrivals may have a considerable impact on the inversion result and may partly explain the variability of certain source models. It is therefore essential to use a reliable velocity model to limit its impact on the final result.

2.4. The inverse problem

The inverse problem consists of finding a slip model $\mathbf{m}$ from the data $\mathbf{d}_{\rm obs}$, from our formulation of the forward problem and our prior knowledge of the model. There are many books that detail the different approaches used to solve the inverse problem. We will only present a few approaches here to introduce regularized optimization and Bayesian inversion. For further details, the reader can refer to [TAR 05].

Here, we consider approaches where an L^2 norm is used to characterize data residuals. We define the data misfit function as:

$$\chi(\mathbf{m}) = \|\mathbf{d}_{\rm obs} - \mathbf{G}(\mathbf{m})\|_2^2 \tag{2.21}$$

The data vector $\mathbf{d}_{\rm obs}$ is generally constructed by concatenating seismic waveforms and other observations (geodetic data, tsunami waveforms, etc.). The problem can also be

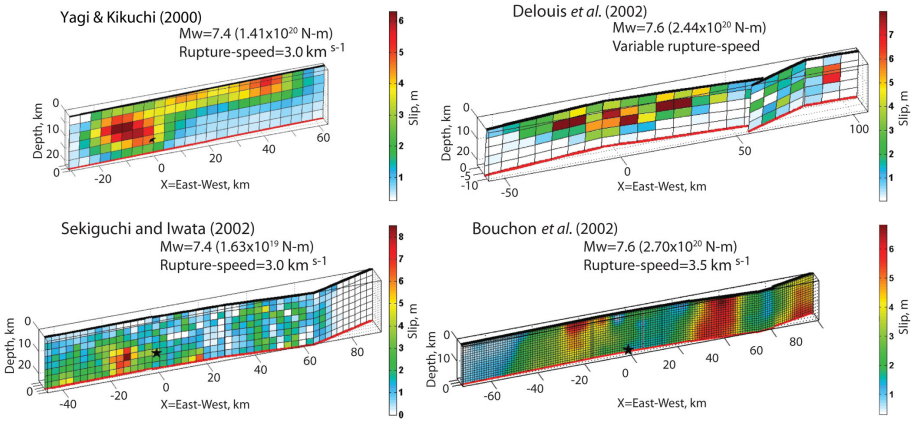

Figure 2.9. An illustration of the variability in kinematic source models. *Slip inversion results obtained by different teams for the 1999 Izmit earthquake. These source models are available through the SRCMOD database [MAI 12]. Figure modified from [DUP 14].*

solved by representing seismological data in the frequency domain. However, as we will see in Section 2.4.3, modeling the data in the frequency domain is theoretically identical to modeling it in the time domain [IDE 07].

Since data is affected by measurement errors and our limited knowledge of the Earth structure, the solution to the inverse problem is usually non-unique. There are usually several slip models associated with a similar data misfit $\chi(\mathbf{m})$. Even when the uncertainty is small, the use of data collected at the Earth's surface to characterize complex ruptures at depth is a fundamentally ill-posed problem. For example, if we consider the linear Gaussian case $\mathbf{G}(\mathbf{m}) = \mathbf{G}\mathbf{m}$, considering independent and identically distributed data, the minimization of $\chi(\mathbf{m})$ leads to the least squares solution:

$$\widetilde{\mathbf{m}} = (\mathbf{G}^t\mathbf{G})^{-1}\mathbf{G}^t\mathbf{d}_{\text{obs}} \tag{2.22}$$

where the superscript t denotes the transposition of a matrix. During slip inversion, the matrix $\mathbf{G}^t\mathbf{G}$ is generally poorly conditioned such that there exists an infinite number of solutions $\widetilde{\mathbf{m}}$ minimizing the data misfit. This variability in the inversion results is depicted in Figure 2.9 in the case of the 1999 Izmit (Turkey) earthquake ($M_W = 7.6$). The 1999 Izmit earthquake is not an isolated case. For many events, small differences in the data set or in the formulation of the problem lead to large differences in the slip distributions [MAI 12]. A widely-used practice to mitigate the non-uniqueness of the solution is to regularize the inversion to obtain a well-conditioned optimization problem. An alternative approach is to characterize the ensemble of plausible models that fit the observations while considering the prior knowledge we already have on the rupture. Both of these approaches are described below.

2.4.1. *Tikhonov regularization approach*

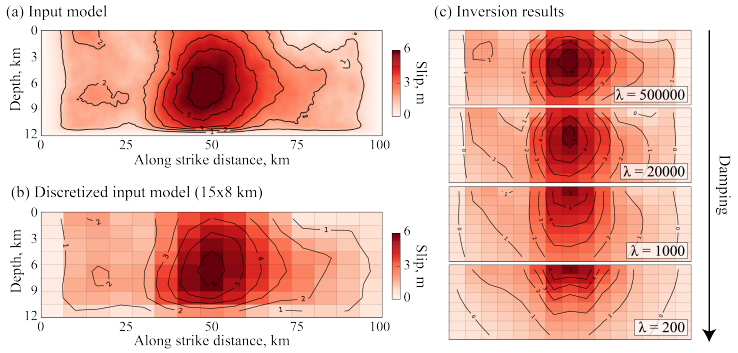

Figure 2.10. Impact of regularization on the slip models. *(a) Synthetic model describing a heterogeneous slip distribution. (b) Synthetic model discretized into rectangular subfaults of 15x8 km. (c) Result of the inversion considering an increasing level of damping. This test was carried out assuming a regularly spaced network of GNSS stations every 10 km around the fault. The smoothing is controlled by the damping λ as indicated in equation (2.23).*

Tikhonov regularization is a widely-used regularization method used to solve ill-posed inverse problems. This method is also known as the 'ridge regression' method. To limit the non-uniqueness of the solution, a regularization term is introduced into the minimization. The solution is then given by:

$$\widetilde{\mathbf{m}} = \arg\min(\|\mathbf{d}_{\text{obs}} - \mathbf{G}(\mathbf{m})\|_2^2 + \lambda^2 \|\mathbf{\Gamma}\mathbf{m}\|_2^2) \tag{2.23}$$

where $\mathbf{\Gamma}$ is the Tikhonov matrix and λ is a damping parameter. In the above equation, "$\arg\min(f(\mathbf{m}))$" defines the value of $\mathbf{m}$ minimizing the cost function $f(\mathbf{m})$. The matrix $\mathbf{\Gamma}$ can take different forms depending on which model characteristics we wish to emphasize. A conventional choice is $\mathbf{\Gamma} = \mathbf{I}$ which favor models with a low L_2 norm (see, for example [OLS 82]). In the context of slip inversion, this regularization may however bias the models towards low moment magnitudes (by artificially reducing the amplitude of fault slip). Another popular choice is the spatial Laplacian operator $\mathbf{\Gamma} = \nabla^2$, which consists of minimizing the model's 'roughness' in order to obtain a relatively smooth slip distribution over the fault.

We now consider a linear case $\mathbf{d} = \mathbf{G}\mathbf{m}$ as in the static case (section 2.3.1) or when using a multiple time window parametrization (section 2.3.2.1). To deal with the inverse problem, consider the weighted case $\mathbf{W}\mathbf{d} = \mathbf{W}\mathbf{G}\mathbf{m}$ with $\mathbf{W}$ being a diagonal matrix whose elements W_{ii} give the weight associated with the i-th data sample. Equation (2.23) then becomes:

$$\widetilde{\mathbf{m}} = (\mathbf{G}^t\mathbf{W}^2\mathbf{G} + \lambda^2\mathbf{\Gamma}^t\mathbf{\Gamma})^{-1}\mathbf{G}^t\mathbf{W}^2\mathbf{d}_{\text{obs}} \tag{2.24}$$

This equation is not used much in practice as it often leads to solutions that incorporates slip in the negative direction (that is, in the direction opposite to the average slip over the fault). Although the existence of such a phenomenon is debated, it is difficult to imagine such a radical reversal in the slip direction in an stressed environment like the Earth's crust. To limit such oscillations in the model, we then integrate positivity constraints: the minimization of equation (2.23) can then be solved using optimization approaches like non-negative least squares, conjugate gradients or simulated annealing [TAR 05].

The solution to equation (2.23) is a trade-off between data misfit $\|\mathbf{d}_{\text{obs}} - \mathbf{G}(\mathbf{m})\|_2^2$ and model regularization $\|\mathbf{\Gamma m}\|_2^2$ whose relative weight is controlled by the damping parameter (λ). The choice of λ thus has a direct impact on the solution. As illustrated in Figure 2.10, a high value of λ will lead to a very smooth model while a lower value of λ will favor a better fit to the data. The most widely used approach consists of using an *L*-curve representing the data misfit $\|\mathbf{d}_{\text{obs}} - \mathbf{G}(\mathbf{m})\|_2^2$ as a function of the model regularization $\|\mathbf{\Gamma m}\|_2^2$ obtained for various values of λ. The idea is then to choose a value of λ at the corner of the curve (offering an acceptable compromise). This choice however remains quite arbitrary and has a significant impact on the resulting slip model (cf., [CAU 10]).

2.4.2. *Bayesian approach*

The Tikhonov regularization is a practical tool to quickly solve slip inversion as an optimization problem. However, this approach is based on model damping, which has no real physical basis. Furthermore, this regularization can also significantly impact the solution (cf., Figure 2.10). The Bayesian approach is a different way to tackle the non-uniqueness of the solution. The idea is to characterize the ensemble of models that can fit the data taking into account the different sources of uncertainty and our *a priori* knowledge of the model. The resulting model ensemble is then considered to be the solution to the inverse problem.

This approach is based on Bayes' theorem to characterize the posterior probability density of the model $\mathbf{m}$ given our observations $\mathbf{d}_{\text{obs}}$:

$$p(\mathbf{m}|\mathbf{d}_{\text{obs}}) = \frac{p(\mathbf{d}_{\text{obs}}|\mathbf{m})p(\mathbf{m})}{p(\mathbf{d}_{\text{obs}})} \tag{2.25}$$

In this equation, $p(\mathbf{m})$ is the probability distribution representing our *a priori* knowledge of the model $\mathbf{m}$. The term $p(\mathbf{d}_{\text{obs}}|\mathbf{m})$ is the data likelihood, representing the plausibility of our observations $\mathbf{d}_{\text{obs}}$ for different models$\mathbf{m}$. Although the data likelihood is a function of $\mathbf{m}$, it is not a probability density on $\mathbf{m}$ (its integral over $\mathbf{m}$ is also not necessarily equal to one). The denominator in equation (2.25) is a normalization

constant that can be defined as:

$$p(\mathbf{d}_{\text{obs}}) = \int p(\mathbf{d}_{\text{obs}}|\mathbf{m})p(\mathbf{m})d\mathbf{m} \tag{2.26}$$

In a Bayesian framework, the solution to the problem is therefore the *a posteriori* probability distribution $p(\mathbf{m}|\mathbf{d}_{\text{obs}})$. This distribution characterizes the information on the model $\mathbf{m}$ given the observations $\mathbf{d}_{\text{obs}}$, the forward formulation of the problem $\mathbf{G}(\mathbf{m})$, the associated uncertainties, and our hypotheses about the model. Formally, the forward problem can be rewritten by taking into account the associated uncertainties:

$$\mathbf{d}_{\text{obs}} = \mathbf{G}(\mathbf{m}) + \mathbf{e}_d + \mathbf{e}_p \tag{2.27}$$

where $\mathbf{e}_d$ represents observational uncertainty (that is, the measurement error) and $\mathbf{e}_p$ corresponds to the uncertainty associated with the forward problem (due to modeling inaccuracies). Although the uncertainty over a forward problem $\mathbf{e}_p$ is generally neglected, its amplitude may be greater than the data uncertainty $\mathbf{e}_d$. $\mathbf{e}_p$ may arise from the imprecisions in the Earth model used to calculate the Green's function, from an oversimplistic fault geometry, or approximations during the parametrization of the rupture process (cf., section 2.3). The uncertainties $\mathbf{e}_d$ and $\mathbf{e}_p$ are commonly considered as Gaussian (a choice that can be justified through the principle of maximum entropy, given the corresponding covariances [JAY 03]). The likelihood function $p(\mathbf{d}_{\text{obs}}|\mathbf{m})$ in equation (2.25) can thus be written as [TAR 05]:

$$p(\mathbf{d}_{\text{obs}}|\mathbf{m}) = \frac{1}{(2\pi)^{N/2}|\mathbf{C}_\chi|^{1/2}} e^{-\frac{1}{2}[\mathbf{d}_{\text{obs}}-\mathbf{G}(\mathbf{m})]^t \mathbf{C}_\chi^{-1}[\mathbf{d}_{\text{obs}}-\mathbf{G}(\mathbf{m})]} \tag{2.28}$$

where N is the number of observations (the size of the vector $\mathbf{d}_{\text{obs}}$) and $\mathbf{C}_\chi$ is the covariance matrix, defined by:

$$\mathbf{C}_\chi = \mathbf{C}_d + \mathbf{C}_p \tag{2.29}$$

where $\mathbf{C}_d$ and $\mathbf{C}_p$ are the covariance matrices associated with $\mathbf{e}_d$ and $\mathbf{e}_p$, respectively. By using this Gaussian form of the likelihood function, the deviation from the data is characterized by a norm, L^2, as in the equation (2.21). The covariance matrix $\mathbf{C}_d$ associated with the observational uncertainties $\mathbf{e}_d$ can take different forms depending on the data being considered. For example, in the case of seismological data, $\mathbf{C}_d$ characterizes the level of noise at each station as well as the temporal correlation for the filtered data (see, for example [DUP 12]). Different approaches have been developed to construct the covariance matrix, $\mathbf{C}_p$, associated with modeling uncertainties $\mathbf{e}_p$, in particular to account for inaccuracies in the Earth model [DUP 14] and the fault geometry [RAG 18].

Let us now consider the linear case (as in sections 2.3.1 and 2.3.2.1), with an *a priori* Gaussian of the form:

$$p(\mathbf{m}) = \frac{1}{(2\pi)^{M/2}|\mathbf{C}_m|^{1/2}} e^{-\frac{1}{2}(\mathbf{m}-\mathbf{m}_{\text{prior}})^t \mathbf{C}_m^{-1}(\mathbf{m}-\mathbf{m}_{\text{prior}})} \tag{2.30}$$

where M is the number of model parameters (i.e., the size of the vector $\mathbf{m}$), $\mathbf{m}_{\text{prior}}$ is the average prior model and $\mathbf{C}_m$ is the *a priori* covariance matrix. In this configuration, the posterior distribution is Gaussian [TAR 05]:

$$p(\mathbf{m}|\mathbf{d}_{\text{obs}}) = \frac{1}{(2\pi)^{M/2}|\widetilde{\mathbf{C}}_m|^{1/2}} e^{-\frac{1}{2}(\mathbf{m}-\widetilde{\mathbf{m}})^t \widetilde{\mathbf{C}}_m^{-1}(\mathbf{m}-\widetilde{\mathbf{m}})} \tag{2.31}$$

where $\widetilde{\mathbf{m}}$ is the posterior average model (also corresponding to the *maximum a posteriori* model) and $\widetilde{\mathbf{C}}_m$ and the posterior covariance which are respectively written as :

$$\begin{aligned} \widetilde{\mathbf{m}} &= (\mathbf{G}^t\mathbf{C}_\chi^{-1}\mathbf{G} + \mathbf{C}_m^{-1})^{-1}(\mathbf{G}^t\mathbf{C}_\chi^{-1}\mathbf{d}_{\text{obs}} + \mathbf{C}_m^{-1}\mathbf{m}_{\text{prior}}) \\ \widetilde{\mathbf{C}}_m &= (\mathbf{G}^t\mathbf{C}_\chi^{-1}\mathbf{G} + \mathbf{C}_m^{-1})^{-1} \end{aligned} \tag{2.32}$$

The linear Gaussian case is useful as it offers an analytical solution to the Bayesian formulation of the inverse problem. The term $\mathbf{C}_m^{-1}$ in equation (2.32) acts as a regularization term. It is interesting to note that by considering $\mathbf{m}_{\text{prior}} = \mathbf{0}$, $\mathbf{C}_\chi^{-1} = \mathbf{W}^2$ and $\mathbf{C}_m^{-1} = \lambda^2\mathbf{\Gamma}^t\mathbf{\Gamma}$, we obtain the regularized least squares solution in equation (2.24). In the linear Gaussian case, there is thus a clear link between the Bayesian formulation and the Tikhonov regularization. If the weighing matrix $\mathbf{W}$ is chosen in an ad hoc manner, the damping parameter λ can also be seen as the ratio between the *a priori* variance in the model and the uncertainty over the data. Furthermore, one of the pieces of information that we have *a priori* is the positivity of fault slip in a given direction (from long-term observations or from the slip orientation expected from the relative motion of the tectonic plates). Some of our parameters are thus associated with a non-Gaussian prior $p(\mathbf{m})$ (typically a uniform distribution defined to be positive), which prevent the use of equations (2.31) and (2.32). Furthermore, there is no analytical form for $p(\mathbf{m}|\mathbf{d}_{\text{obs}})$ in the case of a non-linear problem, like when we invert for rupture velocity and rise time when dealing with kinematic data (cf., section 2.3.2.2).

To solve the problem in the general (non-linear and/or non-Gaussian) case, a sampling approach can be used. Bayesian sampling consists of generation a population of models that will be statistically distributed according to $p(\mathbf{m}|\mathbf{d}_{\text{obs}})$. The solution is thus composed of a set of models distributed with a probability density that is greater when these models fit the observations and are plausible with respect to the *a priori* information $p(\mathbf{m})$. The *a posteriori* distribution will be obtained by generating a large number of samples of models for which $p(\mathbf{m}|\mathbf{d}_{\text{obs}})$ is evaluated. Despite a high cost in terms of computation time, this approach is of interest for ill-posed problems as it does not require the evaluation of the inverse of $\mathbf{G}$ (or of $\mathbf{G}^t\mathbf{G}$). Unlike what is described in equations (2.24) and (2.32), it is thus not necessary to regularize the inversion of $\mathbf{G}$ by smoothing the model or minimizing its L_2 norm. The prior information contained in $p(\mathbf{m})$ must include all physical constraints applicable to the model. Let us take the example of an earthquake for which we wish to find the fault slip distribution. If long-period seismic moment tensor solutions reveal that this is a strike-slip earthquake

of magnitude 7, we can choose an *a priori* distribution for the slip in the rake direction such as $p(\mathbf{m}) = \mathcal{U}(-1m, 15m)$, that is, a uniform distribution between -1 and 15 meters of slip. We do not expect to have more than 15 m of slip for this magnitude and the fault is forbidden from slipping more significantly in the opposite direction. All slip values between -1 and 15 m are, *a priori*, equiprobable. This choice of an *a priori* that gives very little information allows to reduce the explored model space while still allowing the data to drive the posterior solution. This is one of the advantages of Bayesian sampling. For further information on Bayesian sampling for slip inversion, the reader can consult [MIN 13].

2.4.3. *Modeling data in the frequency domain or as wavelets*

In most slip inversion approaches, the data vector $\mathbf{d}_{\text{obs}}$ is constructed by concatenating seismological waveforms with other data sets (GNSS, InSAR, tsunami etc.). The problem can also be solved by representing seismological data in the frequency domain [OLS 88, COT 95] or after wavelet transform [JI 02]. It is shown here that modeling seismological data in these different domains (time, frequency or wavelet) should lead to identical slip models [IDE 07].

We begin by rewriting the misfit function in equation (2.21) in the form:

$$\chi(\mathbf{m}) = \left[\mathbf{d}_{\text{obs}} - \mathbf{G}(\mathbf{m})\right]^t \mathbf{C}_\chi^{-1} \left[\mathbf{d}_{\text{obs}} - \mathbf{G}(\mathbf{m})\right] \tag{2.33}$$

In the following, the inverse of the covariance matrix $\mathbf{C}_\chi$ can invariably be replaced by the weighing matrix $\mathbf{W}^2$ used in equation (2.24). It must also be noted that $\chi(\mathbf{m})$ appears in the Gaussian likelihood function introduced in equation (2.28). The Fourier transform or wavelet transform can be represented by a linear operator $\mathbf{T}$. We can then define:

$$\begin{aligned} \hat{\mathbf{d}}_{\text{obs}} &= \mathbf{T}\mathbf{d}_{\text{obs}} \\ \hat{\mathbf{G}}(\mathbf{m}) &= \mathbf{T}\mathbf{G}(\mathbf{m}) \end{aligned} \tag{2.34}$$

In this equation, $\hat{\mathbf{d}}_{\text{obs}}$ and $\hat{\mathbf{G}}(\mathbf{m})$ correspond to the Fourier/wavelet transform of the data $\mathbf{d}_{\text{obs}}$ and predictions $\mathbf{G}(\mathbf{m})$ in the time domain. It is considered here that $\mathbf{T}$ is an orthonormal operator, such that:

$$\mathbf{T}^t\mathbf{T} = \mathbf{T}\mathbf{T}^t = \mathbf{I} \tag{2.35}$$

where $\mathbf{I}$ is the identity matrix. This is indeed the case for the Fourier transform and also usually the case with the wavelet transforms commonly used in source inversion. The misfit function can thus be defined in the frequency/wavelet domain as:

$$\hat{\chi}(\mathbf{m}) = \left[\hat{\mathbf{d}}_{\text{obs}} - \hat{\mathbf{G}}(\mathbf{m})\right]^t \mathbf{C}_{\widehat{d}}^{-1} \left[\hat{\mathbf{d}}_{\text{obs}} - \hat{\mathbf{G}}(\mathbf{m})\right] \tag{2.36}$$

where $\mathbf{C}_{\widehat{d}}$ is the frequency/wavelet covariance matrix that can be obtained from the covariance $\mathbf{C}_d$ in the time domain by using:

$$\mathbf{C}_{\widehat{d}} = \mathbf{T}\mathbf{C}_d\mathbf{T}^t \tag{2.37}$$

By inserting equations (2.34) and (2.37) into equation (2.36) and then using equation (2.35), it can be shown that:

$$\begin{aligned}\hat{\chi}(\mathbf{m}) &= \left[\mathbf{T}\mathbf{d}_{\text{obs}} - \mathbf{T}\mathbf{G}(\mathbf{m})\right]^t \left(\mathbf{T}\mathbf{C}_d\mathbf{T}^t\right)^{-1} \left[\mathbf{T}\mathbf{d}_{\text{obs}} - \mathbf{T}\mathbf{G}(\mathbf{m})\right] \\ &= \left[\mathbf{d}_{\text{obs}} - \mathbf{G}(\mathbf{m})\right]^t \mathbf{T}^t\mathbf{T}\mathbf{C}_d^{-1}\mathbf{T}^t\mathbf{T} \left[\mathbf{d}_{\text{obs}} - \mathbf{G}(\mathbf{m})\right] \\ &= \left[\mathbf{d}_{\text{obs}} - \mathbf{G}(\mathbf{m})\right]^t \mathbf{C}_d^{-1} \left[\mathbf{d}_{\text{obs}} - \mathbf{G}(\mathbf{m})\right] \\ &= \chi(\mathbf{m})\end{aligned} \tag{2.38}$$

The equality between the misfit functions $\chi(\mathbf{m}) = \hat{\chi}(\mathbf{m})$ for the same model $\mathbf{m}$ shows that the data inversion in the time domain or frequency domain theoretically lead to identical solutions. Of course, this is only valid if the covariance matrices $\mathbf{C}_{\widehat{d}}$ and $\mathbf{C}_d$ are statistically consistent (that is, if equation (2.37) is true). Representing the data in frequency/wavelets makes it possible to easily associate different weights with different frequency bands [JI 02]. In practice, this is done by constructing $\mathbf{C}_{\widehat{d}}$ in the frequency domain. However, it is still possible to carry out the inversion in the time domain by using equation (2.37) to calculate the corresponding covariance matrix $\mathbf{C}_d$.

2.5. Characterization of the source and implications on the physic of earthquakes

The slip models obtained using the methods described above present certain generic properties that are actively debated in literature. In this section, we will examine, in particular, the rupture propagation mode, the rupture velocity, the stress-drop and the energy partitioning of earthquakes.

An interesting property of kinematic models is that they generally show the existence of a slip pulse, corresponding to a narrow slipping band propagating on the fault with a width that is small with respect to the total rupture size [HEA 90]. This observation has important implications on the stress state and friction of faults. Figure 2.11 depicts an example in the case of the 2017 Ezgeleh earthquake in Iran ($M_W = 7.3$). This model shows that a slip pulse quickly appears: in less than 4 s and less than 7 km away from the epicenter (Figure 2.11d). If this pulse were controlled by the rupture size, we would get a rise time of $r = 0.5 \times W/V_R$, where W is the fault width [DAY 82]. Figure 2.11b shows that we systematically have $r < 0.5 \times W/V_R$, which indicates that the pulse appears before the rupture front reaches the edges of the fault. This is known as a self-healing slip pulse [HEA 90]. These narrow pulses can be caused by different factors such as the fault frictional properties, stress heterogeneities, or

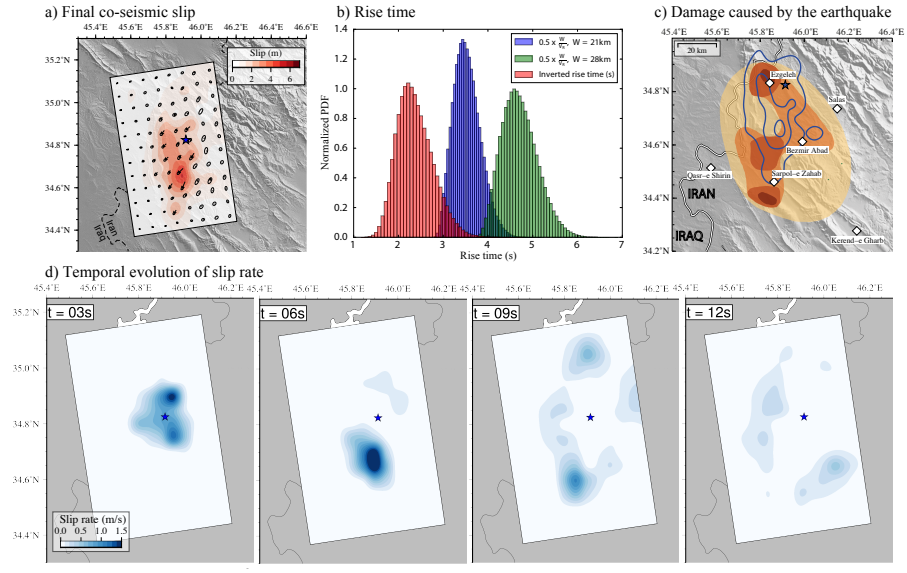

Figure 2.11. Slip pulse during the 2017 Ezgeleh earthquake in Iran ($M_W = 7.3$)**.** *a) Final slip. The colors and arrows indicate slip amplitude and direction. The ellipses represent 95% of posterior uncertainties. The star indicates the location of the hypocenter. b) Comparison of the estimated rise time with the prediction by [DAY 82]. The histogram in red is the a posteriori distribution of rise-time r averaged along the rupture. The histograms in blue and green correspond to predictions according to $r = 0.5 \times W/V_R$ with V_R being the estimated rupture velocity along the rupture, and W being the width of the fault. Two cases are considered: $W = 21$ km (corresponding to 3 sub-faults) and $W = 28$ km (corresponding 4 sub-faults). c) Damage caused by the earthquake. The colors indicate the level of damage estimated by the Iranian geological department. Darkest colors indicate a most severe damage. The blue lines correspond to contour lines of the final slip distribution (every 1.5 m). d) Evolution of the slip velocity over the fault 3, 6, 9 and 12 s after the origin time. Figure modified from [GOM 19].*

wave reflections in the low velocity zone around the fault [COC 94, PEY 01, HUA 11]. The existence of pulse-like ruptures also has implications in terms of seismic hazard and the generation of strong motions. In the case of the Ezgeleh earthquake, the high slip rate, short rise-time and strong directivity of the rupture towards the south seem to have exacerbated the damage to the south of the hypocenter (cf., Figure 2.11c). These slip pulses can be difficult to stop as they involve large dynamic stresses at the rupture front. These ruptures can thus propagate in weakly loaded regions or re-rupture fault zones that were recently broken by another earthquake [VAL 14].

The rupture velocity V_R is also a parameter that can be extracted from kinematic models and which can provide interesting information on the rupture dynamics.

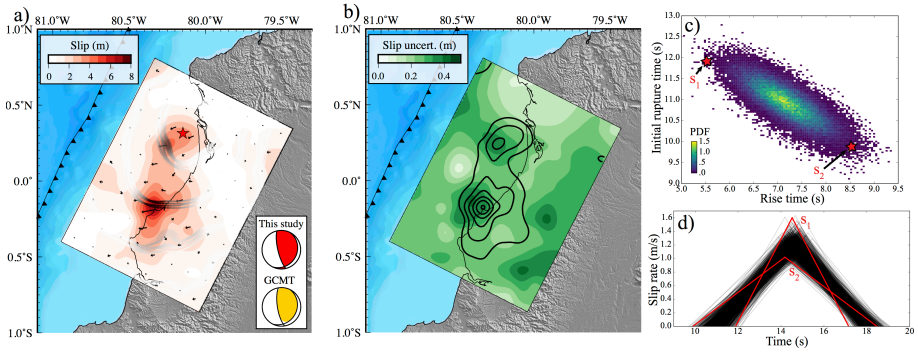

Figure 2.12. Bayesian model of the 2016 Pedernales earthquake in Ecuador ($M_W = 7.8$). *a) Final slip. The colors and arrows indicate the amplitude and direction of slip. The grey lines indicate the stochastic rupture fronts derived from the posterior ensemble of models and displayed at 10, 20 and 30 s. The red star indicates the hypocenter location. b) Final slip uncertainty. c) Marginal a posteriori distribution of rise-time and rupture time in the first slip asperity (located close to the epicenter). d) Corresponding posterior ensemble of local slip rate functions. The source time functions denoted s_1 and s_2 correspond to the rupture time and rise-time indicated by red stars in sub-figure c. Figure modified from [GOM 18b].*

However, V_R and the associated rupture times τ are often estimated with high uncertainty. Figure 2.12 depicts an example of the Bayesian kinematic model obtained for the 2016 Pedernales earthquake ($M_W = 7.8$, Ecuador). We clearly see a tradeoff between rupture time τ and rise-time r with a negative correlation between the two parameters. This is due to the fact that the centroid time of the slip pulse is relatively well-constrained while band-pass filtered data have a limited sensitivity to the initial rupture time and to the local slip duration. While it is generally difficult to restrain the local rupture velocity, the average rupture speed is generally easier to characterize (especially if observations are available at small epicentral distances). Typically, the observed rupture velocities are of the order of 70% of the velocity of the S wave speed around the fault [IDE 07]. However, for certain earthquakes, we see rupture velocities that exceed the S wave velocities. This is theoretically possible for mode II ruptures, that is, when the fault slips in the same direction as the rupture propagation. In practice, these *supershear* ruptures were mainly observed for strike-slip earthquakes [BOU 08, SOC 19] but have also been reported for other kinds of focal mechanisms [ZHA 14].

For periods smaller than 2 s (that is, wavelengths smaller than $\sim$5 km), the heterogeneity of the medium and the rupture complexities produce waveforms that are too complex to be explained by simple models [KAN 04b]. In particular, the observation of complex waveforms at stations located very close to the source suggests significant heterogeneities in the rupture process [ZEN 94]. Given the use of data filtered at low frequency and the spatial smoothing of slip distributions, many kinematic models

inform us about the large wavelength distribution of fault slip. Moreover, sources of high-frequency radiation are not necessarily co-localized with zones with large slip on the fault. For example, the emission of high-frequency waves can be associated with variations in rupture velocity [MAD 77]. Dynamic damage caused by seismic ruptures around the fault may also explain part of the high-frequency content observed at short epicentral distances [THO 17]. At the level of the subduction zones, several studies report the existence of high-frequency sources in the deeper part of the seismogenic domain [SIM 11, LAY 15, GRA 15]. This observation potentially expresses an increased level of frictional and stress heterogeneity at depth [LAY 15].

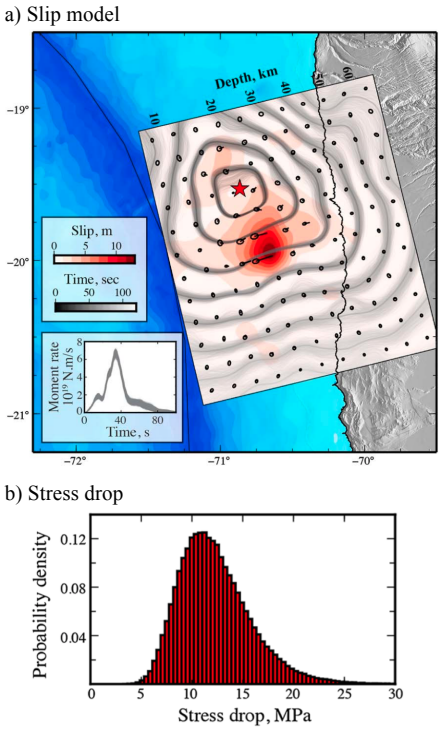

Figure 2.13. Kinematic model of the 2014 Iquique earthquake in Chile ($M_W = 8.1$). *a) Final slip. Colors and arrows indicate the amplitude and direction of slip. The ellipses represent 95% of a posteriori uncertainty. Grey lines indicate the stochastic rupture fronts derived from the posterior ensemble of models (the grey colormap indicate the corresponding rupture time). The red star indicates the location of the hypocenter. The lower left inset shows the posterior ensemble of moment rate functions. b) A posteriori distribution of the average stress drop (See equation 2.40). Modified from [DUP 15].*

The final slip distribution gives direct information on the stress drop caused by the rupture. The final slip distribution is thus commonly used to characterize the average drop in the static stress $\overline{\Delta\sigma}$ associated with an earthquake. A widely-used approach in seismological is based on the seismic moment M_0 and the rupture area A:

$$\overline{\Delta\sigma} = C\frac{M_0}{A^{3/2}} \tag{2.39}$$

where C is a geometric parameter depending on shape of the ruptured zone [NOD 13]. However, in practice, it is often difficult to determine the ruptured area A. For example, the spatial smoothing of the model ($\|\mathbf{\Gamma m}\|$ in equation 2.23) can induce zones with low slip, which are generally poorly constrained. The area A is thus often defined from the regions where the slip exceeds a fraction s_{th} of the maximum slip. Nonetheless, this approach remains problematic as the estimated value of $\overline{\Delta\sigma}$ strongly depends on the chosen threshold s_{th}. An alternative approach is to calculate the co-seismic change in traction $\Delta\sigma$ at the center of each sub-fault (using the [OKA 92] formulation, for example). In the case where the parametrization is based on continuous and differentiable base function, the continuous distribution of $\Delta\sigma$ can also be evaluated. We then express the average stress drop [NOD 13]:

$$\overline{\Delta\sigma} = \frac{\int \mathbf{\Delta u}\, \mathbf{\Delta\sigma} d\Sigma}{\int \mathbf{\Delta u}\, \mathbf{e}_1 d\Sigma} \tag{2.40}$$

where $\mathbf{e}_1$ is the unit vector along the mean slip direction, and $\mathbf{\Delta u}$ is the final distribution of the co-seismic slip. An example of estimation of $\overline{\Delta\sigma}$ based on this approach is presented for the 2014 Iquique earthquake ($M_w = 8.1$) in Figure 2.13. Despite a non-negligible uncertainty, the values estimated between 5 and 25 MPa indicate that the earthquake source is quite compact (the global stress drop average being situated around 3 MPa [ALL 09]).

The spatio-temporal distribution of slip can also be used as a boundary condition for calculating the evolution of stress change during the rupture [BOU 97]. This allows to analyze slip-stress relationships and thus to explore the fault weakening. However, several studies show that the detail of this relation is actually poorly constrained by the filtered data and the parametrization used for kinematic modeling [GUA 00]. On the other hand, the fracture energy E_G, which corresponds to the integral of the stress-slip curve above the level of dynamic friction, is often well characterized by the observations [TIN 05a]. E_G corresponds to the energy dissipated by many processes, such as plastic deformation at the head of the fissure, the creation of micro-cracks outside the fault, fluid pressurization etc. [KAN 06]. Similarly, slip models allows to estimate the energy E_R radiated by earthquakes in the form of seismic waves [RIV 05]. By combing these various observables, it is possible to evaluate energy partitioning during seismic ruptures. During an earthquake, the potential energy (elastic strain energy and gravitational energy) stored in the Earth during the inter-seismic period is released in the form of radiated energy E_R, fracture energy E_G, and frictional energy E_F

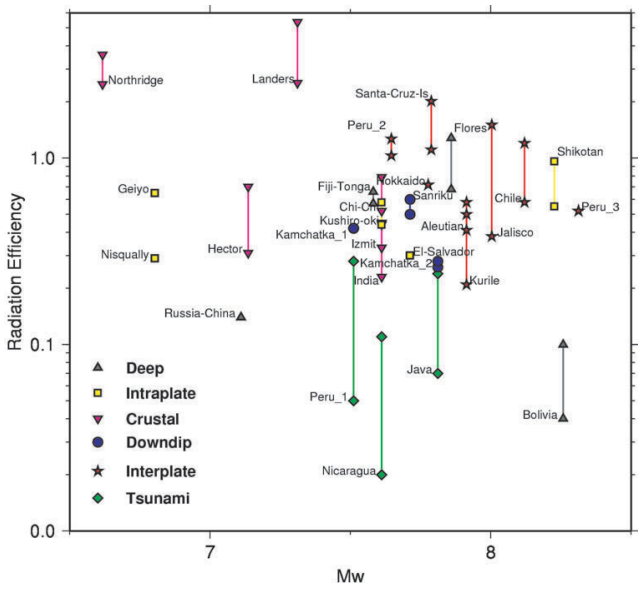

Figure 2.14. Radiation efficiency estimated for several large earthquakes. *The radiation efficiency $\eta_R = \frac{E_R}{E_R+E_G}$ is presented in terms of the moment magnitude M_W. The different symbols correspond to different types of earthquakes (deep, inter-plate, crustal etc.) Figure modified from [VEN 04]*

[KAN 06]. The frictional energy E_F corresponds to the work against the resistance to slip on the fault and is mainly dissipated as heat. There is little information available on E_F, since the seismological data does not provide information regarding the level of absolute stress on the fault. For this reason, we generally focus on the partitioning of the energy available for the rupture propagation $E_{T0} = E_R + E_G$ in terms of radiated energy E_R and fracture energy E_G. In particular, we can estimate the ratio between radiated energy E_R and this available energy E_{T0} from the different parameters that can be derived from slip models:

$$\eta_R = \frac{E_R}{E_R + E_G} \sim \frac{2\mu}{\overline{\Delta\sigma}} \frac{E_R}{M_0} \tag{2.41}$$

where μ is the shear modulus around the fault, $\overline{\Delta\sigma}$ is the average stress drop (cf., equation 2.40) and M_0 is the scalar seismic moment. This parameter, η_R, called the radiation efficiency, is useful in characterizing the overall dynamic behavior of an earthquake. If $\eta_R = 1$, the earthquake is very efficient at radiating seismic energy. If $\eta_R = 0$, the available energy (E_{T0}) is fully dissipated mechanically and there is no radiated energy (such as for slow-slip events discussed in Chapter 7). Figure 2.14 shows η_R for different earthquakes for which this parameter could be estimated. It can be seen that most earthquakes have η_R values greater than 0.25. However, some

earthquakes have a very low radiation efficiency ($\eta_R < 0.25$). This is the case with tsunami earthquakes, which correspond to very slow ruptures that generate tsunamis that are abnormally large with respect to their magnitude. These earthquakes could thus be associated with large dissipative processes. One possible interpretation is that most tsunami earthquakes involve ruptures in deformable sediments at a shallow depth and that a large part of available energy is used for the deformation of these materials. Certain deep earthquakes (at depths > 600 km) are also associated with a $\eta_R < 0.25$, like the 1994 Bolivia earthquake. The mechanics of these earthquakes is not yet well-understood, but these events could involve significant dissipation related to plastic deformation [KAN 98]. On the other hand, high values of η_R for many superficial earthquakes suggests low fracture energy E_G, with important implications concerning these ruptures. In a velocity weakening model, these high values of η_R suggest a small weakening distance (in other words, rapid weakening in terms of slip [KAN 04b]). This also suggests easy runaway ruptures that can easily grow and are difficult to stop.

2.6. Conclusion

In this chapter, we have introduced the most common methods of characterizing the spatio-temporal history of seismic ruptures. There are two broad categories of approaches to describe the evolution of slip on the fault. The first category is based on the linear decomposition of slip evolution into a series of basis functions. This method, called the multiple time window method, is very flexible, but is based on a large number of parameters and can therefore lead to artificially complex models [IDE 07]. The second category of methods is based on the estimation of rupture times and the local duration of slip over the fault. Despite the non-linearity of this approach, possibly associated with the existence of local minima, it usually promotes relatively simple models that can appropriately fit the data. To make optimal use of both types of approaches, certain methods combine the multiple time window method with the non-linear inversion of rupture times in each sub-fault [DEL 02].

Despite using an increasing amount of data to constrain models, slip inversion remains a fundamentally ill-posed problem. Indeed, it is common to have several slip model that fit the observations equally well. Different strategies exist to address such non-uniqueness of the solution. A widely-used approach consists of regularizing the inversion through spatial and/or temporal smoothing of the slip distribution to obtain a well-conditioned optimization problem. This approach is convenient as it allows to rapidly solve the inverse problem. However, it is based on model damping that may have a large impact on the solution. An alternative approach is to restrict ourselves to hypotheses that are *a priori* simple and physically justified, but which do not necessarily guarantee the uniqueness of the solution. This then require characterizing the set of plausible models that fit the data, given these *a priori* constraints. Although this Bayesian approach allows to characterize the uncertainty of the models, it remains

computationally expensive and the ensemble of models is often difficult to visualize in practice.

Slip inversion approaches are commonly used today to characterize earthquake sources. Preliminary kinematic models are now published just a few hours after the occurrence of a large earthquake. These rapid estimates are generally based only on teleseismic data, with a limited resolution of the rupture process. Obtaining better constrained results requires the incorporation of additional data, particularly in the near field. Models now incorporate a large amount of observations, such as broadband and strong-motion seismological data, as well as GNSS, InSAR and optical data, that yield detailed information about ground deformation. An important limitation for underwater earthquakes is the loss of resolution when we move farther away from the coast (most observations being on land). To overcome this problem, it is important to incorporate tsunami data that provide essential information on seafloor displacements. Additionally, the deployment of seafloor observational networks is an important task to improve our understanding of the seismic source.

The improvement of observational and modeling methods enables a constant improvement of slip models and thereby a better understanding of seismic ruptures. Despite these improvements, slip inversion results remain uncertain leading to variability in the models obtained by different teams. For many earthquakes, the accuracy on the estimated source parameters is not enough to draw definitive conclusions on the rupture dynamics. In this context, the estimation of model uncertainty is essential to objectively assess the robustness of our information about the rupture process. A better understanding of earthquake dynamics also requires the development of models that can fit observations over a wide range of frequencies (from static displacements to the high-frequency wavefield).

2.7. Bibliographie

[AAG 13] AAGAARD B. T., KNEPLEY M. G., WILLIAMS C. A., « A domain decomposition approach to implementing fault slip in finite-element models of quasi-static and dynamic crustal deformation », *J. Geophys. Res.: Solid Earth*, vol. 118, n° 6, p. 3059–3079, juin 2013.

[AKI 02] AKI K., RICHARDS P. G., *Quantitative Seismology*, University Science Books, Sausalito, CA, 2nd édition, 2002.

[ALL 09] ALLMANN B. P., SHEARER P. M., « Global variations of stress drop for moderate to large earthquakes », *J. Geophys. Res.*, vol. 114, n° B1, pageB01310, janvier 2009.

[ALL 14] ALLGEYER S., CUMMINS P., « Numerical tsunami simulation including elastic loading and seawater density stratification », *Geophys. Res. Lett.*, vol. 41, n° 7, p. 2368–2375, avril 2014.

[AVO 14] AVOUAC J.-P., AYOUB F., WEI S., AMPUERO J.-P., MENG L., LEPRINCE S., JOLIVET R., DUPUTEL Z., HELMBERGER D., « The 2013, Mw 7.7 Balochistan earthquake, energetic strike-slip reactivation of a thrust fault », vol. 391, n° 0, p. 128–134, 2014.

[BOU 76] BOUCHON M., « Teleseismic body wave radiation from a seismic source in a layered medium », *Geophys. J. Int.*, vol. 47, n° 3, p. 515–530, décembre 1976.

[BOU 81] BOUCHON M., « A simple method to calculate Green's functions for elastic layered media », *Bull. Seism. Soc. Am.*, vol. 71, n° 4, p. 959–971, août 1981.

[BOU 97] BOUCHON M., « The state of stress on some faults of the San Andreas System as inferred from near-field strong motion data », *J. Geophys. Res.*, vol. 102, n° B6, p. 11731–11744, juin 1997.

[BOU 08] BOUCHON M., KARABULUT H., « The Aftershock Signature of Supershear Earthquakes », *Science*, 2008.

[BÜR 14] BÜRGMANN R., CHADWELL D., « Seafloor Geodesy », *Annual Review of Earth and Planetary Sciences, Vol 43*, vol. 42, n° 1, p. 509–534, mai 2014.

[CAU 10] CAUSSE M., COTTON F., MAI P. M., « Constraining the roughness degree of slip heterogeneity », *J. Geophys. Res.*, vol. 115, n° B5, pageB05304, mai 2010.

[COC 94] COCHARD A., MADARIAGA R., « Dynamic faulting under rate-dependent friction », *Pure appl. geophys.*, vol. 142, n° 3, p. 419–445, septembre 1994.

[COT 95] COTTON F., CAMPILLO M., « Frequency domain inversion of strong motions: Application to the 1992 Landers earthquake », *J. Geophys. Res.*, vol. 100, page3961, 1995.

[DAY 82] DAY S. M., « Three-dimensional finite difference simulation of fault dynamics: Rectangular faults with fixed rupture velocity », *Bull. Seism. Soc. Am.*, vol. 72, n° 3, p. 705–727, juin 1982.

[DEL 02] DELOUIS B., GIARDINI D., LUNDGREN P., SALICHON J., « Joint Inversion of InSAR, GPS, Teleseismic, and Strong-Motion Data for the Spatial and Temporal Distribution of Earthquake Slip: Application to the 1999 İzmit Mainshock », *Bull. Seism. Soc. Am.*, vol. 92, n° 1, p. 278–299, février 2002.

[DUP 12] DUPUTEL Z., RIVERA L., FUKAHATA Y., KANAMORI H., « Uncertainty estimations for seismic source inversions », *Geophys. J. R. astr. Soc.*, vol. 190, n° 2, p. 1243–1256, août 2012.

[DUP 14] DUPUTEL Z., AGRAM P. S., SIMONS M., MINSON S. E., BECK J. L., « Accounting for prediction uncertainty when inferring subsurface fault slip », *Geophys. J. Int.*, vol. 197, n° 1, p. 464–482, avril 2014.

[DUP 15] DUPUTEL Z., JIANG J., JOLIVET R., SIMONS M., RIVERA L., AMPUERO, RIEL B., OWEN S. E., MOORE A. W., SAMSONOV S. V., CULACIATI F. O., MINSON S. E., « The Iquique earthquake sequence of April 2014: Bayesian modeling accounting for prediction uncertainty », *Geophys. Res. Lett.*, vol. 42, n° 19, p. 7949–7957, octobre 2015.

[DUP 17] DUPUTEL Z., RIVERA L., « Long-period analysis of the 2016 Kaikoura earthquake », *Phys. Earth Planet. Inter.*, vol. 265, p. 62–66, avril 2017.

[GOM 18a] GOMBERT B., DUPUTEL Z., JOLIVET R., DOUBRE C., RIVERA L., SIMONS M., « Revisiting the 1992 Landers earthquake: a Bayesian exploration of co-seismic slip and off-fault damage », *Geophys. J. Int.*, vol. 212, n° 2, p. 839–852, février 2018.

[GOM 18b] GOMBERT B., DUPUTEL Z., JOLIVET R., SIMONS M., JIANG J., LIANG C., FIELDING E. J., RIVERA L., « Strain budget of the Ecuador-Colombia subduction zone: A stochastic view », *Earth Planet. Sci. Lett.*, vol. 498, p. 288–299, 2018.

[GOM 18c] GOMBERT B., Vers une nouvelle génération de modèles de glissements cosismiques : analyse stochastique et approche multi-données, PhD thesis, Université de Strasbourg, mars 2018.

[GOM 19] GOMBERT B., DUPUTEL Z., SHABANI E., RIVERA L., JOLIVET R., HOLLINGSWORTH J., « Impulsive Source of the 2017 MW=7.3 Ezgeleh, Iran, Earthquake », *Geophys. Res. Lett.*, vol. 46, n° 10, p. 5207–5216, mai 2019.

[GRA 15] GRANDIN R., VALLÉE M., SATRIANO C., LACASSIN R., KLINGER Y., SIMOES M., BOLLINGER L., « Rupture process of the Mw7.9 2015 Gorkha earthquake (Nepal): Insights into Himalayan megathrust segmentation », vol. 42, n° 20, p. 8373–8382, octobre 2015.

[GUA 00] GUATTERI M., SPUDICH P., « What can strong-motion data tell us about slip-weakening fault-friction laws? », *Bull. Seism. Soc. Am.*, vol. 90, n° 1, p. 98–116, février 2000.

[HAR 78] HARTZELL S. H., « Earthquake aftershocks as Green's functions », *Geophys. Res. Lett.*, vol. 5, n° 1, p. 1–4, janvier 1978.

[HEA 90] HEATON T. H., « Evidence for and implications of self-healing pulses of slip in earthquake rupture », *Phys. Earth Planet. Inter.*, vol. 64, n° 1, p. 1–20, novembre 1990.

[HER 13] HERRMANN R. B., « Computer Programs in Seismology: An Evolving Tool for Instruction and Research », *Seismol. Res. Lett.*, vol. 84, n° 6, p. 1081–1088, novembre 2013.

[HJÖ 09] HJÖRLEIFSDÓTTIR V., KANAMORI H., TROMP J., « Modeling 3-D wave propagation and finite slip for the 1998 Balleny Islands earthquake », *J. Geophys. Res.*, vol. 114, pageB03301, 2009.

[HUA 11] HUANG Y., AMPUERO J.-P., « Pulse-like ruptures induced by low-velocity fault zones », *Journal of Geophysical Research: Solid Earth (1978–2012)*, vol. 116, n° B12, pageB04301, décembre 2011.

[IDE 07] IDE S., « Slip Inversion », *Treatise on Geophysics*, vol. 4, p. 193–223, janvier 2007.

[INA 13] INAZU D., SAITO T., « Simulation of distant tsunami propagation with a radial loading deformation effect », *Earth Planets Space*, vol. 65, n° 8, p. 835–842, août 2013.

[JAY 03] JAYNES E. T., *Probability Theory: The Logic of Science*, Cambridge university press, New York, 2003.

[JI 02] JI C., WALD D. J., HELMBERGER D. V., « Source Description of the 1999 Hector Mine, California, Earthquake, Part I: Wavelet Domain Inversion Theory and Resolution Analysis », *Bull. Seism. Soc. Am.*, vol. 92, n° 4, p. 1192–1207, mai 2002.

[JOH 12] JOHNSON K. M., FUKUDA J., SEGALL P., « Challenging the rate-state asperity model: Afterslip following the 2011 M9 Tohoku-oki, Japan, earthquake », *Geophys. Res. Lett.*, vol. 39, n° 20, pageL20302, octobre 2012.

[JOL 11] JOLIVET R., GRANDIN R., LASSERRE C., DOIN M.-P., PELTZER G., « Systematic InSAR tropospheric phase delay corrections from global meteorological reanalysis data », *Geophys. Res. Lett.*, vol. 38, n° 17, p. n/a–n/a, septembre 2011.

[KAN 98] KANAMORI H., ANDERSON D. L., HEATON T. H., « Frictional Melting During the Rupture of the 1994 Bolivian Earthquake », *Science*, vol. 279, n° 5352, p. 839–842, février 1998.

[KAN 04a] KANAMORI H., « The diversity of the physics of earthquakes », *Proc. Jpn. Acad.*, vol. 80, n° 1, p. 297–316, 2004.

[KAN 04b] KANAMORI H., BRODSKY E. E., « The physics of earthquakes », *Reports on Progress in Physics*, vol. 67, n° 8, p. 1429–1496, août 2004.

[KAN 06] KANAMORI H., RIVERA L., « Energy Partitioning During an Earthquake », *Radiated Energy and the Physics of Faulting, Geophys. Monogr. Ser.*, p. 3–13, American Geophysical Union, Washington D. C., 2006.

[KAN 10] KANEKO Y., AVOUAC J.-P., LAPUSTA N., « Towards inferring earthquake patterns from geodetic observations of interseismic coupling », *Nature Geosci.*, vol. 3, n° 5, p. ngeo843–369, avril 2010.

[KIK 91] KIKUCHI M., KANAMORI H., « Inversion of complex body waves–III », *Bull. Seism. Soc. Am.*, vol. 81, n° 6, page2335, décembre 1991.

[KLE 17] KLEIN E., VIGNY C., FLEITOUT L., GRANDIN R., JOLIVET R., RIVERA E., METOIS M., « A comprehensive analysis of the Illapel 2015 Mw8.3 earthquake from GPS and InSAR data », *Earth Planet. Sci. Lett.*, vol. 469, p. 123–134, 2017.

[KOM 99] KOMATITSCH D., TROMP J., « Introduction to the spectral element method for three-dimensional seismic wave propagation », *Geophys. J. Int.*, vol. 139, n° 3, p. 806–822, décembre 1999.

[LAR 03] LARSON K. M., BODIN P., GOMBERG J., « Using 1-Hz GPS data to measure deformations caused by the Denali fault earthquake », *Science*, vol. 300, n° 5624, p. 1421–1424, 2003.

[LAY 81] LAY T., KANAMORI H., *An Asperity Model of Large Earthquake Sequences*, American Geophysical Union, 1981.

[LAY 15] LAY T., « The surge of great earthquakes from 2004 to 2014 », *Earth Planet. Sci. Lett.*, vol. 409, p. 133–146, janvier 2015.

[LIU 98] LIU P. L. F., WOO S.-B., CHO Y.-S., « Computer Programs for Tsunami Propagation and Inundation », Cornell University, USA, 1998.

[MAD 77] MADARIAGA R., « High-frequency radiation from crack (stress drop) models of earthquake faulting », *Geophys. J. R. astr. Soc.*, vol. 51, n° 3, p. 625–651, décembre 1977.

[MAI 12] MAI M., « Source Inversion Validation (SIV): Current Results & Developments », *2012 SCEC Source Inversion Validation Workshop*, 2012.

[MAS 93] MASSONNET D., ROSSI M., CARMONA C., ADRAGNA F., PELTZER G., FEIGL K., RABAUTE T., « The displacement field of the Landers earthquake mapped by radar interferometry », *Nature*, vol. 364, p. 138–142, juillet 1993.

[MIN 13] MINSON S. E., SIMONS M., BECK J. L., « Bayesian inversion for finite fault earthquake source models I—theory and algorithm », vol. 194, n° 3, p. 1701–1726, juin 2013.

[NOC 17] NOCQUET J. M., JARRIN P., VALLÉE M., MOTHES P. A., GRANDIN R., ROLANDONE F., DELOUIS B., YEPES H., FONT Y., FUENTES D., REGNIER M., LAURENDEAU A., CISNEROS D., HERNANDEZ S., SLADEN A., SINGAUCHO J. C., MORA H., GOMEZ J., MONTES L., CHARVIS P., « Supercycle at the Ecuadorian subduction zone revealed after the 2016 Pedernales earthquake », *Nature Geosci.*, vol. 10, n° 2, p. 145–149, février 2017.

[NOD 13] NODA H., LAPUSTA N., KANAMORI H., « Comparison of average stress drop measures for ruptures with heterogeneous stress change and implications for earthquake physics », *Geophys. J. Int.*, vol. 193, n° 3, p. 1691–1712, juin 2013.

[OKA 85] OKADA Y., « Surface deformation due to shear and tensile faults in a half-space », *Bull. Seism. Soc. Am.*, vol. 75, p. 1135–1154, 1985.

[OKA 92] OKADA Y., « Internal deformation due to shear and tensile faults in a half-space », *Bull. Seism. Soc. Am.*, vol. 82, p. 1018–1040, 1992.

[OLS 82] OLSON A. H., APSEL R. J., « Finite Faults and Inverse-Theory with Applications to the 1979 Imperial-Valley Earthquake », *Bull. Seism. Soc. Am.*, vol. 72, n° 6, p. 1969–2001, 1982.

[OLS 88] OLSON A. H., ANDERSON J. G., « Implications of frequency-domain inversion of earthquake ground motions for resolving the space-time dependence of slip on an extended fault », *Geophys. J. Int.*, vol. 94, n° 3, p. 443–455, septembre 1988.

[PEY 01] PEYRAT S., OLSEN K., MADARIAGA R., « Dynamic modeling of the 1992 Landers earthquake », *Journal of Geophysical Research: Solid Earth (1978–2012)*, vol. 106, n° B11, p. 26467–26482, novembre 2001.

[RAG 18] RAGON T., SLADEN A., SIMONS M., « Accounting for uncertain fault geometry in earthquake source inversions – I: theory and simplified application », *Geophys. J. Int.*, vol. 214, n° 2, p. 1174–1190, mai 2018.

[RIV 05] RIVERA L., KANAMORI H., « Representations of the radiated energy in earthquakes », *Geophys. J. Int.*, vol. 162, n° 1, p. 148–155, juillet 2005.

[SAT 07] SATAKE K., « 4.17 - Tsunamis », *Treatise on Geophysics*, p. 483–511, Elsevier, Amsterdam, 2007.

[SCH 98] SCHOLZ C. H., « Earthquakes and friction laws », *Nature*, vol. 391, n° 6662, p. 37–42, janvier 1998.

[SIM 07] SIMONS M., ROSEN P. A., « 3.12 - Interferometric Synthetic Aperture Radar Geodesy », *Treatise on Geophysics*, Elsevier, Amsterdam, 2007.

[SIM 11] SIMONS M., MINSON S. E., SLADEN A., ORTEGA F., JIANG J., OWEN S. E., MENG L., AMPUERO J.-P., WEI S., CHU R., HELMBERGER D. V., KANAMORI H., HETLAND E., MOORE A. W., WEBB F. H., « The 2011 Magnitude 9.0 Tohoku-Oki Earthquake: Mosaicking the Megathrust from Seconds to Centuries », *Science*, vol. 332, n° 6036, p. 1421–1425, juin 2011.

[SLA 08] SLADEN A., HÉBERT H., « On the use of satellite altimetry to infer the earthquake rupture characteristics: Application to the 2004 Sumatra event », vol. 172, n° 2, p. 707–714, février 2008.

[SOC 19] SOCQUET A., HOLLINGSWORTH J., PATHIER E., BOUCHON M., « Evidence of supershear during the 2018 magnitude 7.5 Palu earthquake from space geodesy », *Nature Geosci.*, vol. 12, n° 3, p. 192–199, mars 2019.

[TAR 05] TARANTOLA A., *Inverse Problem Theory and Methods for Model Parameter Estimation*, SIAM, Philadelphia, 2005.

[THO 17] THOMAS M. Y., BHAT H. S., KLINGER Y., « Effect of Brittle Off-Fault Damage on Earthquake Rupture Dynamics », *Fault Zone Dynamic Processes*, p. 255–280, John Wiley & Sons, Inc., Hoboken, NJ, USA, juin 2017.

[TIN 05a] TINTI E., SPUDICH P., COCCO M., « Earthquake fracture energy inferred from kinematic rupture models on extended faults », *J. Geophys. Res.: Solid Earth*, vol. 110, n° B12, 2005.

[TIN 05b] TINTI E., FUKUYAMA E., PIATANESI A., COCCO M., « A Kinematic Source-Time Function Compatible with Earthquake Dynamics », *Bull. Seism. Soc. Am.*, vol. 95, n° 4, p. 1211–1223, août 2005.

[TRI 74] TRIFUNAC M. D., « A three-dimensional dislocation model for the San Fernando, California, earthquake of February 9, 1971 », *Bull. Seism. Soc. Am.*, vol. 64, n° 1, p. 149–172, février 1974.

[TSA 13] TSAI V. C., AMPUERO J.-P., KANAMORI H., STEVENSON D. J., « Estimating the effect of Earth elasticity and variable water density on tsunami speeds », *Geophys. Res. Lett.*, vol. 40, n° 3, p. 492–496, février 2013.

[TWA 19] TWARDZIK C., VERGNOLLE M., SLADEN A., AVALLONE A., « Unravelling the contribution of early postseismic deformation using sub-daily GNSS positioning », *Scientific Reports*, vol. 9, n° 1, p. 1–12, février 2019.

[VAL 14] VALLÉE M., SATRIANO C., « Ten year recurrence time between two major earthquakes affecting the same fault segment », *Geophys. Res. Lett.*, vol. 41, n° 7, p. 2312–2318, avril 2014.

[VEN 04] VENKATARAMAN A., KANAMORI H., « Effect of directivity on estimates of radiated seismic energy », *J. Geophys. Res.*, vol. 109, n° B4, page1265, avril 2004.

[WAN 18] WANG T., WEI S., SHI X., QIU Q., LI L., PENG D., WELDON R. J., BARBOT S., « The 2016 Kaikoura earthquake: Simultaneous rupture of the subduction interface and overlying faults », *Earth Planet. Sci. Lett.*, vol. 482, p. 44–51, 2018.

[WEI 13] WEI S., HELMBERGER D., ZHAN Z., GRAVES R., « Rupture complexity of the Mw 8.3 sea of okhotsk earthquake: Rapid triggering of complementary earthquakes? », *Geophys. Res. Lett.*, vol. 40, n° 19, p. 5034–5039, octobre 2013.

[YOK 20] YOKOTA Y., ISHIKAWA T., « Shallow slow slip events along the Nankai Trough detected by GNSS-A », *Science Advances*, vol. 6, n° 3, pageeaay5786, janvier 2020.

[ZEN 94] ZENG Y., ANDERSON J. G., YU G., « A composite source model for computing realistic synthetic strong ground motions », *Geophys. Res. Lett.*, vol. 21, n° 8, p. 725–728, avril 1994.

[ZHA 14] ZHAN Z., HELMBERGER D. V., KANAMORI H., SHEARER P. M., « Supershear rupture in a Mw 6.7 aftershock of the 2013 Sea of Okhotsk earthquake », *Science*, vol. 345, n° 6193, p. 204–207, juillet 2014.

[ZHU 02] ZHU L., RIVERA L. A., « A note on the dynamic and static displacements from a point source in multilayered media », *Geophys. J. Int.*, vol. 148, n° 3, p. 619–627, mars 2002.